1	This manuscript is a preprint:
2	
3 4 5 6	This manuscript has been submitted to the Earth and Planetary Science Letters. Subsequent versions of this manuscript may have different content. If accepted, the final version of this manuscript will be available via the 'Peer-reviewed Publication DOI' link via this webpage.
7	
8 9	Please feel free to contact any of the authors directly or to comment on the manuscript. We welcome feedback!
10	
11 12	Note: Supplementary information that is referenced in the text is provided at the bottom of the document.

### 13 Throw rate acceleration caused by dip-linkage on normal faults

- \*Billy J. Andrews<sup>1</sup>, Zoë K. Mildon<sup>1</sup>, Constanza Rodriguez Piceda<sup>1</sup>, Matthew P. Watkinson<sup>1</sup>,
- 15 Craig Magee<sup>2</sup>, Christopher A-L Jackson<sup>3,4</sup>, Mark T. Ireland<sup>5</sup>
- <sup>1</sup> School of Geography, Earth and Environmental Sciences, University of Plymouth, Drake
- 17 Circus, Plymouth, PL4 8AA, UK
- 18 <sup>2</sup> School of Earth and Environment, University of Leeds, Leeds, LS2 9JT, UK
- 19 <sup>3</sup> Landscapes and Basins Research Group (LBRG), Department of Earth Science and
- 20 Engineering, Imperial College, London, SW7 2BP, UK
- <sup>4</sup> WSP UK Ltd, 8 First Street, Manchester, M14 4RP, UK
- <sup>5</sup>School of Natural and Environmental Sciences, Newcastle University, Newcastle upon Tyne,
- 23 UK
- 24 \*Corresponding author.

### 25 Abstract

- Areas of crustal extension often contain pre-existing structures that can reactivate or
- influence the geometry and growth of new, overlying faults. As strain accumulates, it is well
- 28 know that new faults may link down-dip with pre-existing faults. Such linkage invariably
- leads to an increase in fault surface area, which is empirically linked to increasing seismic
- 30 hazard. However, the timescales over which this linkage may occur, and its effects on throw-
- rate evolution and related seismic hazard, are poorly constrained. We use high-resolution 3D
- 32 seismic reflection and borehole data from offshore NW Australia to investigate the growth
- and throw-rate evolution of two normal faults. By mapping age-constrained seismic horizons
- and constructing throw-length and -distance plots we show evidence of growth via dip-

linkage, along all or part of their mapped length. We find that linkage did not occur
simultaneously along the fault, but over a protracted period especially near fault tips. The
absolute timing of fault linkage is influenced by the total throw on the pre-existing fault,
throw accumulation rates during subsequent rifting, position along the fault, and the
intervening stratigraphic thickness. Progressive dip-linkage increases fault surface area and is
associated with an increase in throw-rate on linked segments. Given these effects on fault
geometry and displacement patterns, we argue that dip-linkage should be integrated into fault
growth models and considered in seismic hazard assessments in rifted regions with inherited
structures.

- Keywords (up to 7): Normal fault, Rifting, Structural inheritance, Fault reactivation, Slip-
- 45 rate

35

36

37

38

39

40

41

42

43

44

### 46 Highlights (1-5, max 85 characters inc. spaces)

- 1. We use throw-depth plots to investigate dip-linkage and throw-rate evolution
- 48 2. Dip-linkage occurred at different times at different positions along the fault
- 49 3. A protracted linkage history was observed close to the fault tips
- 4. Dip-linkage was found to be comtomparanous to an increase in throw-rate
- 5. Variable dip-linkage age has implications for models of fault growth and seismic
- 52 hazard assessment

### Data statement

- Well reports and seismic data can be accessed through https://portal.ga.gov.au/).
- 55 DUG Insight software (v.5.1, 2021) was used for seismic visualisation, interpretation and
- 56 analysis.

### 57 Achnowledgements

- We would like to thank DugInsight for the provision of an academic license for their software
- 59 package.
- This work was supported by a UKRI Future Leaders Fellowship MR/T041994/1 (PI Z.
- 61 Mildon).

### 1. Introduction

62

63 Large normal faults have the potential to cause damaging and life-threatening earthquakes. 64 Because earthquake magnitude is partly controlled by fault size, and the recurrence interval 65 directly related to a faults slip rate, forecasting and mitigating seismic hazards rely on 66 acquisition of accurate fault dimension (length, height) and slip or throw rate data (Pace et al., 67 2016). Throw rate and fault dimensions can, however, evolve during extension (Nicol et al., 2005; Rotevatn et al., 2019). For example, fault size, and throw distribution and rates, may 68 69 either remain constant over millions of years (Nicol et al., 1997) or exhibit temporal 70 variability across a range of timescales due to for example, earthquake clustering 71 (Coppersmith, 1988; Kagan and Jackson, 1991), fault linkage (e.g., Dawers and Anders, 72 1995; Peacock, 2002; Rotevatn et al., 2019) stress transfer from nearby faults and/or shear zones (Dolan et al., 2007; Mildon et al., 2022; Mouslopoulou and Hristopulos, 2011), or 73 74 changes in the regional plate extension rate (Nicol et al., 2005). Since throw rate is inversely 75 proportional to earthquake recurrence time, and fault length proportional to maximum 76 earthquake magnitude, an increase or decrease in either will raise or lower, respectively, the 77 hazard posed by a particular fault (e.g., Pace et al., 2016). To improve seismic hazard 78 assessment, we thus need to better understand how fault geometry and throw changes through 79 time and the factors that may influence these changes. The relatively small size of surface 80 exposures, and limited resolution of subsurface geophysical datasets which may lack accurate 81 age constraints on fault-adjacent growth strata, makes it challenging to determine fault 82 dimension, throw patterns, and throw rate evolution. 83 Continental rifts often undergo multiple phases of extension, where faults associated with 84 renewed extension are influenced by structural inheritance from prior extensional phases 85 (Samsu et al., 2023; Deng et al., 2017a; 2017b; Phillips et al., 2018; Faccenna et al., 1995;

Duffy et al., 2015; Collanega et al., 2019; Deng et al., 2021; Phillips et al., 2018). With increasing displacement, faults at different structural levels can propagate towards each other, eventually dip-linking to form a single, larger fault (Collanega et al., 2019; Roche et al., 2021). In cases where the orientation of cover and pre-existing faults are similar, faults may hard link, with a displacement minima preserved at the point where the fault segments joined (e.g., Walsh and Watterson, 1989). These throw minima act as markers on throw-depth plots that reveal the dip-linkage history of a fault and through the integration of high-resolution age data, we have for the first time used throw-minima to gain insights into the spatial-temporal evolution of dip-linkage.

86

87

88

89

90

91

92

93

94

95

96

97

98

99

100

101

102

103

104

105

106

107

108

109

110

The linkage of faults across structural levels through dip-linkage increases the faults overall surface area, which in turn can increase the potential rupture area of an earthquake and their associated magnitudes (Shearer, 2019; Wells and Coppersmith, 1994). While the geometric implications of linkage are well understood, fewer studies have examined the timing of dipfault linkage and how these processes influence throw accumulation rates (Mansfield and Cartwright, 1996; Sun et al., 2022; Yang and Elders, 2016). Understanding the timing and mechanisms of dip-linkage is critical because it may influence when faults reach sizes capable of hosting larger earthquakes and how slip is distributed along faults through time. For example, we might expect dip-linkage to result in spatially variable slip-rate depending on the location and total throw of the pre-existing fault. We use 3D seismic and borehole data from the Exmouth Plateau, offshore NW Australia, to constrain the growth and throw-rate evolution of two now-inactive normal faults that grew through dip-linkage of initially isolated segments (Fig. 1, 2). The multiple rift phases, evidence of rift reactivation across the basin, and high-quality seismic datasets and abundant well data make the Exmouth Plateau an ideal location to test the spatial and temporal evolution of dip-linkage and its effect on throw accumulation. We show that dip-linkage does not occur simultaneously along a faults length,

- but progresses over millions of years, correlating with an increase in throw accumulation rate.
- This indicates that fault linkage strongly influences the growth and seismic potential of
- normal faults through time and that this method offers new insights into the timescales and
- mechanisms of fault linkage across structural levels.

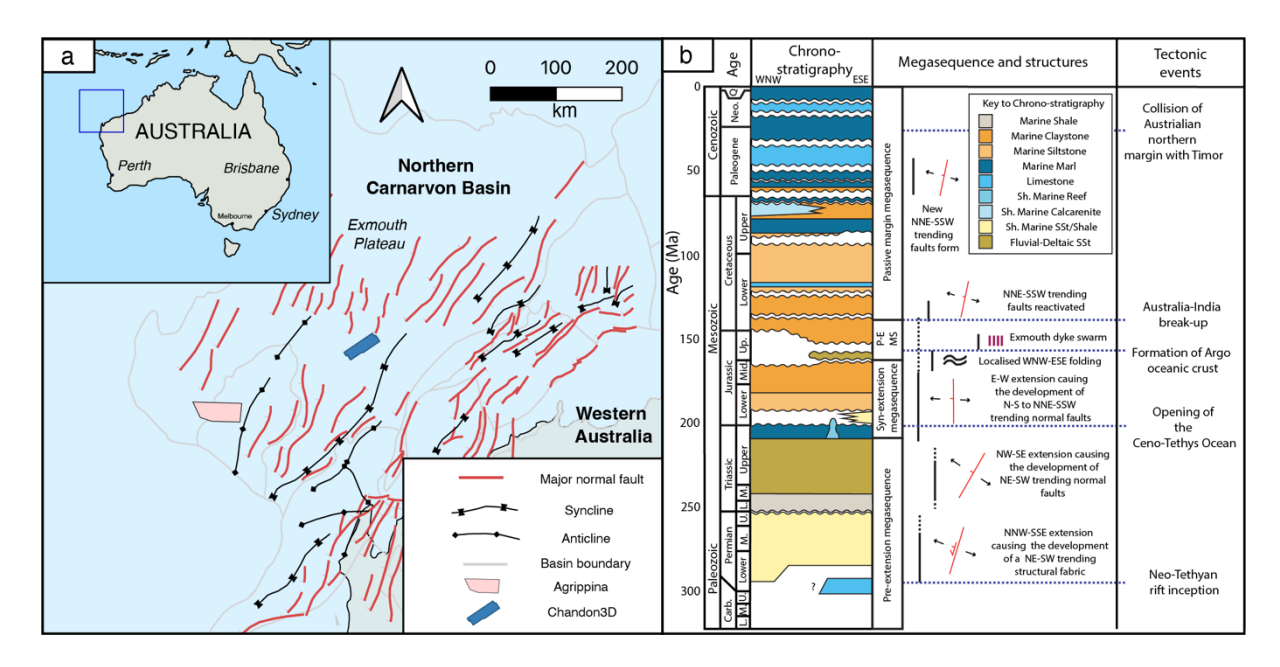


Figure 1: a) Structural elements of the Northerna Carnarvon Basin highlighting the major normal fault trend and location of sub-basins and (b) simplified tectonostratigraphic chart for the central Exmouth Plateau (after Bilal and McClay, 2022).

The studied faults are situated on the Exmouth Plateau, Northern Carnarvon Basin, offshore NW Australia (Fig. 1a). The basin developed through four main phases of rifting and inversion (Deng et al., 2024; Gartrell, 2000; Veevers, 1988) (Fig. 1b). WNW-ESE-directed extension during the Late Carboniferous to Permian established a NNE-trending structural grain, dominated by NW-SE-striking normal and oblique slip faults, across much of the margin, including the Exmouth Plateau (Bilal and McClay, 2022; Deng and McClay, 2021, 2019; Etheridge and O'Brien, 1994; Gartrell, 2000). The stratigraphy offset by and deposited during the very earliest stage of extension is deeper than the record length of both seismic volumes we use here and is therefore not observed. The oldest, deepest growth packages related to the rift-related faults, imaged within our data, are Early to Middle Triassic (~250 to 210 Ma); these are blanketed by Early to Late Triassic interburden stratigraphy (i.e.,

lithologies between successions that show growth strata) (Mungaroo Formation; Bilal and McClay, 2022). Between the Late Triassic and Middle Jurassic (~209.5 to 162.5 Ma), minor E-W extension led to fault propagation folding and localised reactivation of the faults that formed during Late Carboniferous and Early to Middle Triassic rifting (Bilal and McClay, 2022; Karner and Driscoll, 1999; Deng et al., 2024). Although the footwalls of large-throw faults were exposed and degraded at this time (Barrett et al., 2021; Bilal and McClay, 2022), this was not the case for small- to moderate-throw faults (such as F1 and F2, the two faults studied here; Fig. 2), leading to the deposition of strata on both their footwalls and hanging walls. Renewed extension during the Late Jurassic to Early Cretaceous (162.5 to 137.7 Ma) caused the local reactivation of pre-existing faults (Black et al., 2017; Direen et al., 2008). Following continental break-up in the Early Cretaceous (~135 to 130 Ma), faults continued to accommodate small amounts of throw during a phase otherwise dominated by thermal subsidence (Black et al., 2017; Direen et al., 2008).

### 3 Methods and studied faults

### 3.1 Seismic and well data

We use two 3D seismic reflection surveys, Agrippina and Chandon3D, located on the Exmouth Plateau, offshore NW Australia (Fig. 1a). Both surveys are time-migrated, zero-phase processed, SEG reverse polarity, with record lengths of 7.1 and 6 seconds two-way-time (TWT) and bin spacings of 18.75 m × 25 m and 25 m × 25 m, respectively. An estimate of the visibility and separability limits (i.e. vertical resolution) of these data is based on the velocity (1.7 to 3.2 km sec<sup>-1</sup>) and frequency (11.5 to 35.6 Hz) content in the stratigraphic intervals (1.7-7.8 km and 1.3-7.3 km, respectively) of interest (Brown, 2011). For both datasets visibility and separability 3-15 m and 17-70 m, respectively. This resolution is

sufficient to enable the relatively detailed investigation of along-strike pattens of dip-linkage and to image discrete surfaces that can be tied to the chronostratigraphic framework derived from well ties. Crucially, this enables us to determine the throw-rate evolution of the fault. In addition to seismic reflection data, we use two wells located within the Chandon3D (Chandon-1, Chandon-2, Chandon-3) and Agrippina (VOS1) surveys to constrain the age and lithologies of mapped horizons. The wells are drilled into the footwalls of tilted fault blocks and terminate in the upper portion of the Mungaroo Formation. While this adds uncertainty into our analysis, due to the similar seismic properties in the footwall and hanging wall, and the presence of horizons on both the footwall and hanging wall, we believe the lack of wells in the hanging wall will not alter our conclusions. Wells include check shot, formation top depth, gamma ray, sonic, neutron porosity, and bulk density data, which allow the seismic data to be linked to the stratigraphy via the generation of synthetic seismograms. When combined with age data derived from well reports, this allows us to generate a robust, ageconstrained, seismic-stratigraphic framework. Note that we use ages form nearby well reports instead of regional horizon ages for several reasons. Uncertainty in horizon ages exists across the Exmouth Plateau due to poor calibration of dinoflagellate zones and difficulty dating regional unconformities (Reeve et al., 2022). As we are interested in fault linkage trends across single faults and not correlating linkage patterns across the basin and given the age data is used in the calculation of both linkage age and throw-rate, any age discrepancies

between the studied cubes will not impact the conclusions of the study. Another advantage of

using well reports is that they constrain the ages of four reflections in Agrippena within the

augment the age data for the seismic-stratigraphic framework in the Chandon survey area, we

also include three additional horizons (H13, H16, H17) within the Barrow Group (H13) and

Mungaroo Formation (e.g., 205 Ma sandstone), which provide a greater density of age

constrained horizons during the earliest stages of development of the studied fault. To

154

155

156

157

158

159

160

161

162

163

164

165

166

167

168

169

170

171

172

173

174

175

176

177

Mungaroo (H16, H17) Formations by assuming constant sedimentation between horizons of known age (after Lathrop et al., 2021). Whilst this adds some uncertainty to: 1) our throw-rates estimates; and 2) the exact timing of, for example, fault linkage, the use of additional horizons as timelines provides a greater resolution to explore dip-linkage, enabling further trends to be identified.

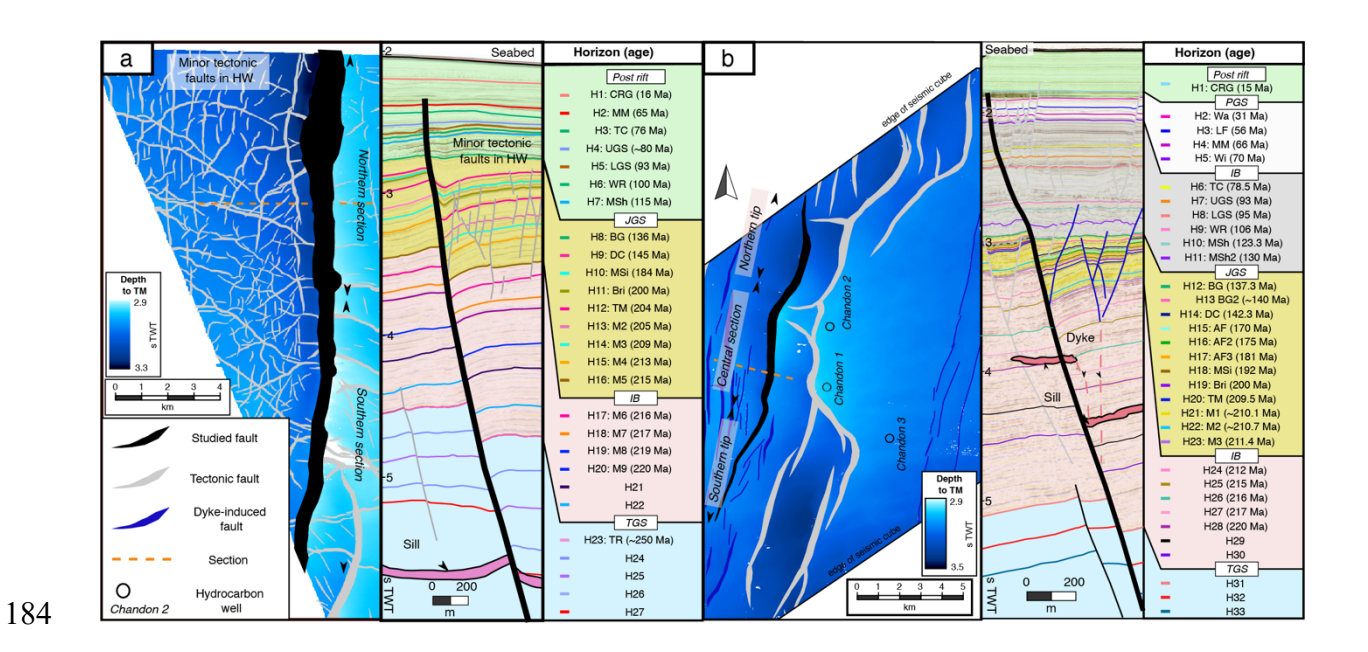


Figure 2: Time-structure map of the Top Mungaroo (TM) and seimic stratigraphy for

(a) Agrippina, which contains Fault 1 and (b) Chandon3D, which contains Fault 2. TGS

= Lower to Middle Triassic growth strata, JGS = Jurassic growth strata, PGS =

Paleogene growth strata, IB = Interburden. Horizon acronyms: CRG = Cape Range

Group, Wa = Walcott Formation, LF = Lambert Formation, MM = Miria Formation,

Wi = Wilcox Formation, TC = Toolonga Calcilutite, UGS = Upper Gearle Formation,

LGS = Upper Gearle Formation, WR = Windalia Radiolarite, MSh = Muderong Shale,

MSh2 = Inter Muderong shale horizon, BG = Barrow Group, BG2 = Inter Barrow

Group horizon, DC = Dingo Claystone, AF = Athol Formation, AF2-3 = Inter Athol

Formation horizons, Msi = Murat Siltstone, Bri = Brigadier Formation, TM = Top

Mungaroo, M1-9 = Inter Mungaroo horizons, TR = regional Triassic reflector

To determine fault throw we measure the vertical distance between horizons offset by and thus cut-off against the studied fault (see below). We convert these cut-off pairs from TWT to meters using seismic velocities estimated from check-shot data from nearby wells (Supplementary 1). Given the interval of interest extends below the wells, velocities are extrapolated by fitting a second-order polynomial to the combined check-shot data for each seismic cube (e.g., Andrews et al., 2024; Lathrop et al., 2021; Magee and Jackson, 2020). However, polynomial curves (and thus velocities) differ between wells; this leads to depth-dependant uncertainty in cut-off depth for horizons in the fault hangingwall (Holden et al., 2024). A sensitivity test using the polynomial curves for each well suggests that changing our depth conversion effects absolute values of fault throw (and thus throw-rate) (Figure S3), but is unlikely to significantly alter the key kinematic trends and our overall conclusions (Table S2). Overall, we expect there to be errors in our exact values to be 10 m for the shallower horizons, and up to 40 m for deeper horizons.

# 3.2 Extracting throw, calculating the timing of fault linkage, and determining throw rate evolution

We measure throw by transposing a fault-perpendicular transect along the fault and sampling every 100 m. To minimise obliquity-related errors, a new transect is constructed if fault strike changes by >15°, whilst ensuring the gaps between samples remains <100 m (Andrews et al., 2024). Horizon cut-offs are picked by projecting the regional horizon dip onto the fault plane in the footwall and hanging wall to obtain cut-off pairs, thereby incorporating non-discrete strain caused by near fault folding and/or sub-seismic brittle deformation (Andrews et al., 2024; Childs et al., 2017; Delogkos et al., 2020; Peacock and Sanderson, 1991; Walsh and Watterson, 1990). Throw is calculated by subtracting the depth-converted footwall cut-off depth from the depth-converted hanging wall cut-off depth.

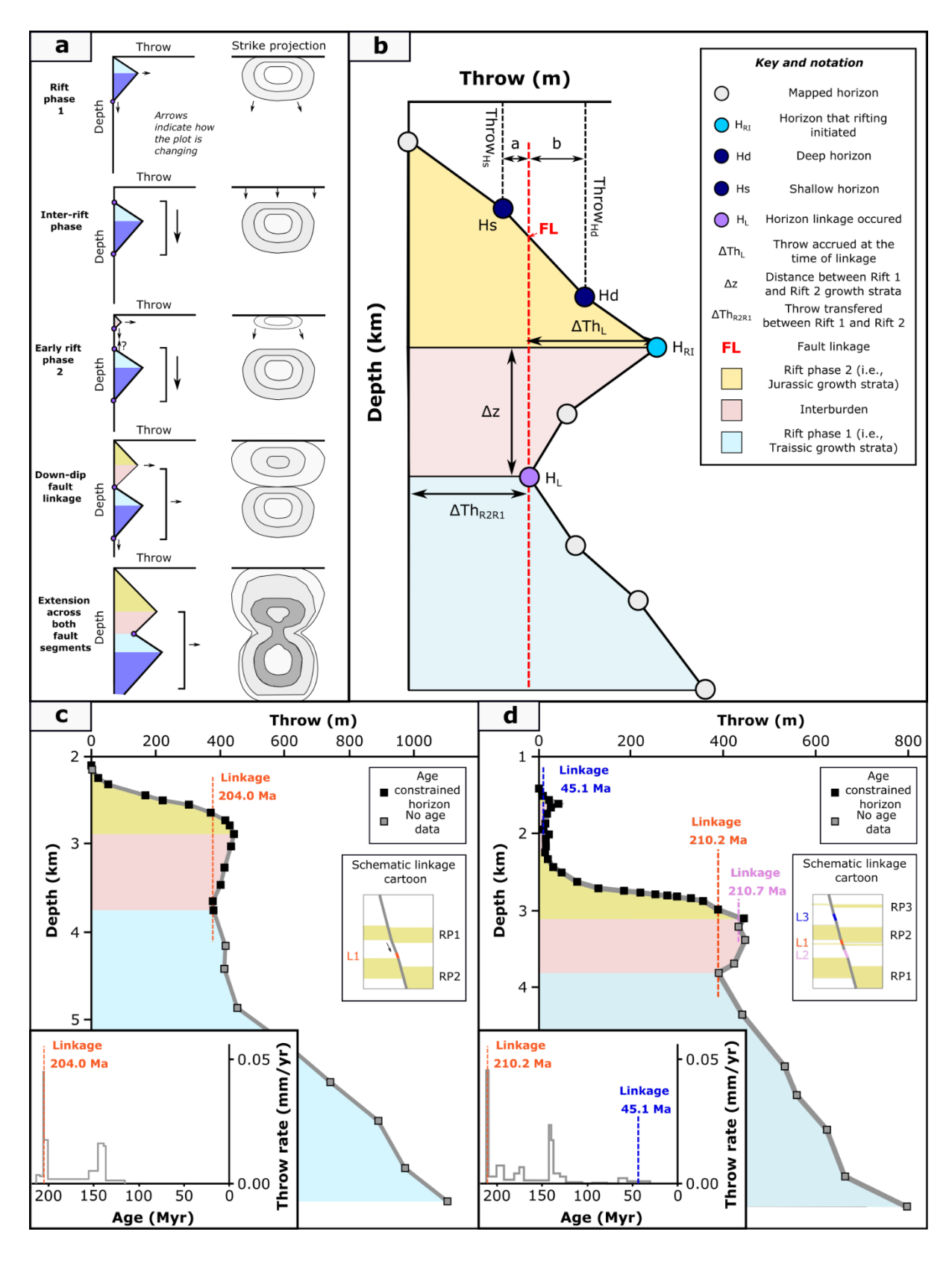


Figure 3: Using throw depth (Tz) plots to calculate linkage age and throw rate. a) evolution of Tz plots during dip-linkage; b) Nomenclature and methodology for estimating fault linkage ages using Tz plots; example Tz plots for (c) F1 and (d) F2. Note

how the 210.7 Ma linkage age could be due to errors in throw extraction, or the linkage of faults that nucleated in the interburden. The insets indicate the slip-rate evolution and age of fault linkage derived from the Tz plot.

224

225

226

227

228

229

230

231

232

233

234

235

236

237

238

239

240

241

242

243

244

245

246

247

We generate throw-depth (Tz) plots at each sample location to explore the role of dip-linkage in fault growth (Jackson and Rotevatn, 2013; Rykkelid and Fossen, 2002). For Tz plots created using horizon picks that are closely spaced in depth, a throw minima is typically assumed to approximate the location where previously isolated fault segments have undergone dip-linkage (i.e., a 'linkage horizon', H<sub>L</sub>) and a throw maxima may approximate the point where a fault segment initiated (i.e., an 'initiation horizon', H<sub>RI</sub>) (Jackson et al., 2017; Walsh and Watterson, 1989). Any portion of the Tz plot where throw increases with depth and the fault is flanked by growth strata likely represents a period of extension. Tz plots that record the dip-linkage of two fault segments are characterised by two areas of relatively large throw, separated by an area of relatively low throw, measured at the linkage horizon (H<sub>L</sub>), that is elongate along fault strike (Jackson et., 2017). At the time of diplinkage, the throw across the linkage horizon(s) will be zero; over the time scales considered in this study, throw will subsequently accumulate across the whole fault, increasing throw on the linkage horizon (H<sub>L</sub>) (Fig 3a). Throw across H<sub>L</sub> reflects post-linkage accumulation, and the difference between the linkage  $(H_L)$  and initiation  $(H_{RI})$  horizons captures pre-linkage throw.

To infer linkage age, we locate the throw across the linage horizon (H<sub>L</sub>) within the upper growth package (e.g., 377 m between H12 and H13; Fig. 3c) and identify the nearest shallower (Hs) and deeper (Hd) horizons. We then calculate the linkage age by assuming consistent throw accumulation between these horizons (i.e., the slope of the T-z plot) using the equation:

248 
$$Age_{Hs} + \left[ (Age_{Hd} - Age_{Hs}) \times \frac{H_L - Throw_{Hs}}{(H_L - Throw_{Hs}) + (Throw_{Hd} - H_L)} \right]$$

where  $Age_{Hs}$  is the age of the shallow horizon,  $Age_{Hd}$  is the age of the deep horizon,  $H_L$  is the throw across the linkage horizon,  $Throw_{Hs}$  is throw across the shallow horizon, and  $Throw_{Hd}$  is throw across the deep horizon. In Figure 3c, the age and throw across the shallow and deep horizons are 204 Ma and 376 m, and 205 Ma and 421 m, respectively, giving a linkage age of 204.0 Ma. Multiple throw minima indicate more than two fault segments have undergone dip-linkage (Fig 23d), enabling multiple linkage ages to be calculated in these cases.

The method described above and in Fig 3 requires three key criteria to be met. First, closely spaced mapped horizons throughout the seismic volume, with corresponding age constraints within the upper growth package. Where this is not the case, and mapped horizons are separated by large vertical distances, uncertainties in linkage age could arise, for example, due to the true depth of fault linkage occurring between mapped horizons. Second, the surface throw on the fault needs to be close to zero at the time of linkage to enable the throw across H<sub>L</sub> to be used to calculate linkage age; this means that the fault needs to be close to, but not breaching, the surface at the time of linkage. Notably, however, some faults were demonstrably surface-breaching during Upper Triassic rifting on the Exmouth Plateau, with many large faults across the Exmouth Plateau show significant footwall degradation (Barrett et al., 2021; Bilal and McClay, 2022). Where this is not taken into account by projecting the regional dip onto the fault plane, the throw across the horizons used to determine linkage age will be lower than the true accumulated throw and cause the linkage age to be underestimated. In cases where there is exposed footwall, if the regional dip is not projected onto the fault plane, a portion of throw across a given horizon will have already occurred by

the time the horizon is deposited. In these cases, the method will underestimate the linkage age. Conversely, where a fault is blind and overlain by a fault-propagation fold, failure to account for this deformation by only measuring discontinuous horizon-fault cut-offs would over-estimate the time where faults became kinematically linked. The final criteria is that sediment accumulation needs to occur along the whole length of the fault throughout the time periods of interest to ensure throw-depth and slip-rate plots accurately represent the faults growth history (Jackson et al., 2017). We therefore suggest only using this method on well-imaged faults that have a good stratigraphic framework, where sedimentation rate exceeds throw rate and where there is no evidence of footwall degradation, and using throw calculated from continuous fault cut-offs. These conditions are met by F1 and F2.

To test whether dip-linkage effects the rate of throw accumulation on the studied faults, we calculate throw-rate for each along-strike sample point. Throw-rate can be calculated when and where sediment accumulation rate exceeds fault throw rate, with this technique having been widely used to explore the long-term evolution of faults (Marsh et al., 2010; Meyer et al., 2002; Nicol et al., 2005; Pan et al., 2022). On a Tz plot, this condition occurs where the gradient is positive, as is the case for the Lower to Middle Triassic and Late Triassic to Middle Jurassic growth packages (Fig 3c, d). Throw rate is calculated as the throw difference between two age-constrained horizons divided by the age difference; this calculation is repeated for each period and each Tz plot. To compare the calculated throw-rates to linkage age, we split F1 into 2 sections (Fig. 4b), and F2 into three sections (Fig. 5b) based on the distribution of linkage ages. For example, in F2, linkage ages occur a protracted time interval towards the southern and northern tips, but occur during two clusters in the central portion (Fig. 5b). By plotting cumulative linkage age against throw-rate for each section, we then visually compare the linkage gradient to changes in throw-rate (Fig 4c-d, 5c-e).

296

297

298

299

300

301

302

303

304

305

306

307

308

309

310

311

312

313

314

315

316

317

### 4.1 General fault structure and related stratigraphy

We examine two faults, F1 and F2, which have a maximum throw of 1447 m and 629 m, respectively (Fig. 2). The studied faults show along-strike differences in geometry and throw. F1 strikes N-S and extends beyond the southern extent of the Agrippina seismic volume, with ~20 km of the fault length imaged (Fig 2a). Throw profiles extracted from horizons within the Upper Triassic to Jurassic growth package have a throw maxima towards the northern extent of the seismic volume; however, throw profiles extracted from horizons within the Lower to Middle Triassic growth package show throw within this interval increases southwards. F2 strikes NNE-SSW and is fully imaged within the seismic cube with a tip-totip length of ~15 km. F2 shows a throw maxima close to the centre of the fault for horizons within both the Lower to Middle Triassic and Upper Triassic to Jurassic growth packages, with the throw distribution slightly skewed towards the north in the latter (Fig 2b). Lower to Middle Triassic and Upper Triassic to Jurassic growth packages are evidenced along the entire length of F1 (Fig 4a), but are missing at the southern tip of F2, where the lower fault tip is observed within the Mungaroo Formation (Fig 5a). The thickness between growth packages varies considerably, from 88 to 1236 m along F1 (average = 487 m) and 79 to 1490 m along F2 (average = 315 m), reflecting spatial variation in both throw and sediment accumulation. In addition to the major growth packages, the central portion of F2 preserves minor post-Mesozoic growth packages (Fig. 5a). Throw minima between growth packages suggest the dip-linkage of initially isolated faults (Fig 3c, d; see also Walsh and Watterson, 1989), facilitating an examination of the along-strike linkage history between these sequences. Now the similarities and differences between the studied faults have been

outlined, we will discuss the linkage history of each fault and how this relates to the throw accumulation rate through time.

### 4.2 F1: Complete hard linkage

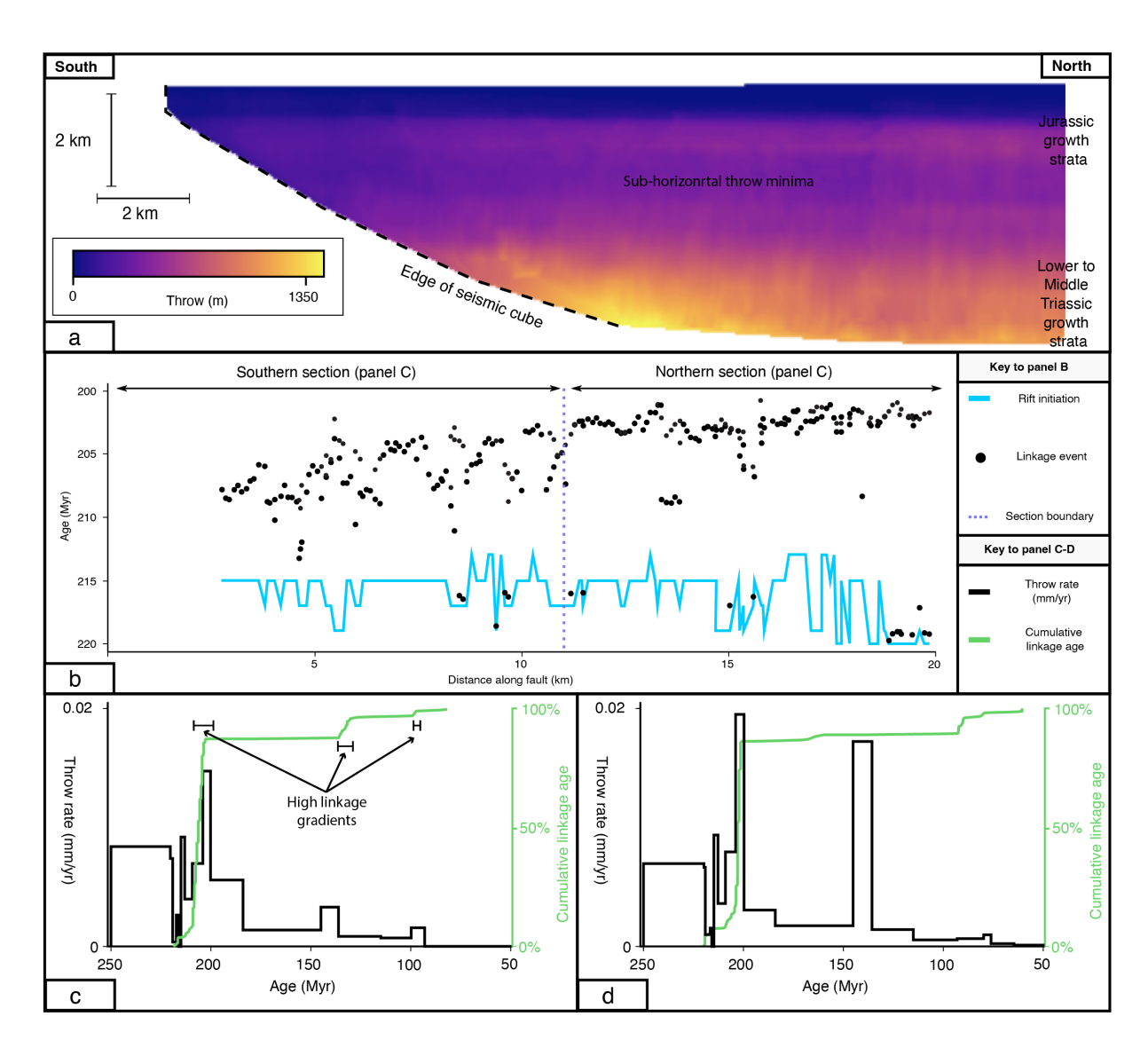


Figure 4: Fault linkage and slip rate history for F1: a) strike projection showing the distribution of throw across F1. b) along-strike distribution of rift initiation (i.e., first recorded throw accumulation on the fault) and fault linkage ages for F1. Note how the linkage ages in south, where the throw in RP1 is higher, are earlier and more spread out when compared to the northern section of the fault. Slip-rate through time and cumulative linkage plots for the (c) southern and (d) northern sections of F1. Note how

linkage occurs rapidly in the southern section of the fault, associated with an acceleration in slip rate. Across both sections, rapid linkage occurs during the period of greatest slip rate (213 to 200 Ma).

328

329

330

331

332

333

334

335

336

337

338

339

340

341

342

343

344

345

346

347

348

349

350

351

The portion of F1 that lies within the seismic cube shows different trends in throw accumulation rate between the Lower to Middle Triassic and Upper Triassic to Jurassic growth packages. Throw accumulation across the Lower Triassic to Middle Triassic growth package continued for longer in the south, with isolated portions of the fault showing growth across the 219 to 217 Ma horizons. This contrasts with the northern portion of the fault, where syn-rift deposition ceased prior to the oldest age-constrained horizons (H20, 220 Ma) (Figure S2.1). Tz plots imply that faulting related to Upper Triassic to Jurassic growth strata initiated between 220 and 213 Ma, with faulting apparently starting slightly earlier in the northern section than the southern section (blue line in Fig 4a). F1 extended beyond the southern limit of the seismic cube within 7 Myr of its initiation (Fig 4b). Having estimated difference in the timing and location of throw accumulation along F1, we now explore the timing and spatial variability of fault linkage events, which differ between the northern and southern sections (Fig 4b). By 200 Ma, most fault linkage had occurred (86% and 87% in the south and north, respectively), with the southern section displaying more along-strike variation in linkage age when compared to the northern section (Fig. 4c, d). Linkage ages partly correlate to minor peaks in the 204 to 200 Ma slip rate profile (Figure S7b), with earlier and later linkage ages corresponding to peaks and troughs in the profile, respectively. This effect is most pronounced in the south, where throw across the Lower to Middle Triassic horizons is greatest and the thickness of strata between the Lower to Middle

Triassic and Upper Triassic to Jurassic growth packages is lowest (Supplementary 4).

Locally, fault linkage began shortly after the initiation of Upper Triassic to Jurassic rifting

(219 to 215 Ma), particularly to the north. For many throw-depth plots where early linkage was identified, a second linkage event is also observed. This later linkage is spatially coincident with to the position of maximum throw within the Upper Triassic to Jurassic growth package (Fig. 4b). Linkage events after 200 Ma, which are often limited in along-strike extent (<1 km), represent the linkage of faults that initiated at shallower structural levels and are not discussed further for F1.

Patterns and rates of throw accumulation on the northern and southern sections are similar (Fig 4c, d). In both sections, faulting initiated at 215 Ma, as defined by the base of the Upper Triassic to Jurassic growth package. During deposition of the earliest, stratigraphically lowest part of this package, both sections were characterised by an initially elevated slip rate (0.009 mm/yr; 215 to 213 Ma), followed by a small decrease (0.004 mm/yr; 213 to 209), and then an acceleration from 209 to 204 Ma (0.008 mm/yr), with the fastest slip rate occurring between 200 and 204 Ma (0.017 mm/yr). The greatest number of linkage ages occurs between 209 to 204 Ma (81%), coinciding with the fastest observed slip rate (Fig 4d, e). An additional increase in throw-rate is observed between 145 and 136 Ma; however, unlike the 209 to 204 Ma time interval there is no associated increase in the number of fault linkage ages (Fig 4d, e).

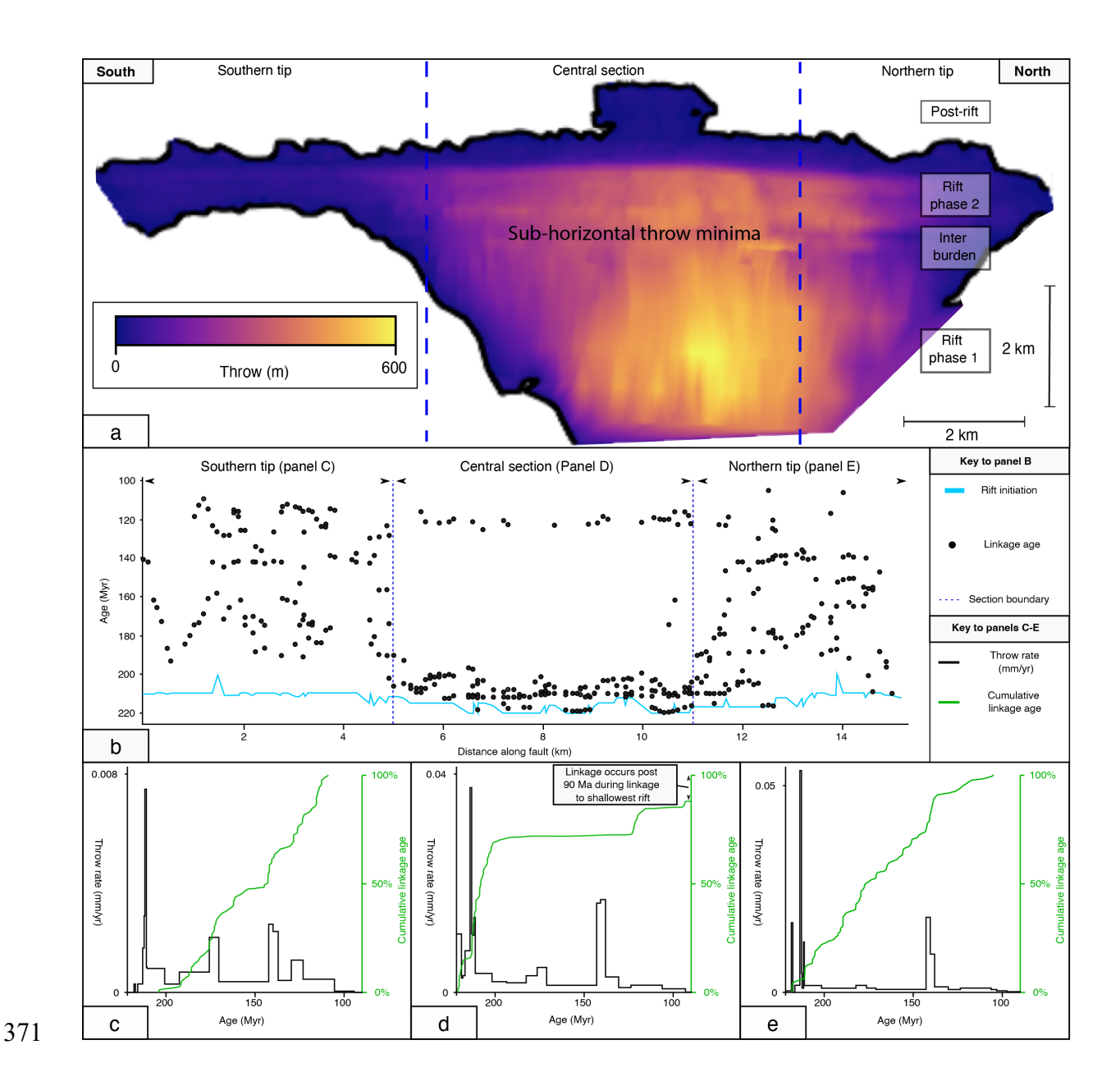


Figure 5: Fault linkage and slip rate history for F2. A) strike projection showing the distribution of throw across F2. B) along-strike distribution of rift initiation and fault linkage ages for F2. Note how F2 initiated earlier in the central section, with rapid fault linkage occurring within 20 Myr of fault slip, whereas fault initiation was later towards the fault tips, with a more protracted linkage history observed. Slip-rate through time and cumulative linkage plots for the (C) southern tip, (D) central section, and (E)

Northern tip of F2. Note how the majority of fault linkage in the central section occurs concurrently with high slip-rate values, and that later slip rate pulses cause linkage towards the fault tips. Note that only linkage events older than 100 Myr are plotted to illustrate the linkage between RP1 and RP2, please see Supplementary 4 for full linkage history of F2.

F2 displays a more complex throw distribution when compared to F1, with the throw pattern differing across both tips and the central section (Fig 5a). The southernmost ~5 km of F2, immediately inboard of the fault tip, is characterised by low throw (<200 m), with the fault tipping out downwards within the Mungaroo Formation (i.e., no Lower to Middle Triassic growth package is observed). This contrasts with the northern tip, where throw increases are observed across both the Lower to Middle Triassic and Upper Triassic to Jurassic growth packages (Fig 5a). The central section displays three broad throw maxima at different structural levels, with evidence of prominent minima observed above and below the Upper Triassic to Jurassic growth package (Fig 5a). Throw-depth plots show that within the Upper Triassic to Jurassic growth package, the central section of the fault initiated first, with an average initiation age of the central section of 217.1 Ma, compared to 213.2 for the northern tip and 211.4 Myr for the southern tip (Fig. 5b). These observations indicate that while the present-day fault length was established within 20 Myr of rifting, fault growth was asymmetrical, with the fault initially propagated northwards.

The linkage history also varies within as well as between different sections of the fault (Fig 5b). In the central section, dip-linkage typically initiated earlier that at the fault tips with 70% of linkage events occurring over 24 Myr (220 to 196 Myr), with further clusters of dip-linkage occurring between 115 and 125 Ma (13%), ~94 Ma (5%) and <55 Ma (12%) (Fig 5b, d). This contrasts with the southern and northern fault tips (Fig 5b, c, e), where dip-linkage

occurred over 93 Myr (202 to 109 Ma) and 112 Myr (206 to 104 Ma) respectively. The northern tip displays a more gradual change from clustered to gradual linkage ages when compared to the southern tip, where limited clustering is observed (Fig 5c). For both tips, linkage typically occurred after >10 Myr of fault activity. Additionally, neither tip shows any geometric interaction (i.e., hard linkage) with faults younger than 100 Myr. This suggests that fault interaction between rift phases differs between areas of high throw (central section), where linkage occurs quickly and over a a shorter time period compared to fault tips, where linkage occurs later and over a greater time period. This leads to the observed elliptical shape of the distacce-age plot (Fig 5b).

There are both similarities and differences in throw rate across the fault sections (Fig 5c-e). Throw rate is the greatest across all sections for time periods after 215 Ma, with the central and northern sections showing greater throw-rates throughout. Despite this, the peaks in the throw-rate through time are similar across all sections. An acceleration in slip-rate occurs between 215 and 211.4 Ma in all sections. During this period, over 50% of recorded linkage events occurring during this time interval. This contrasts with 0 and 10% linkage for the southern and northern tips respectively. Later throw-rate peaks occur at 175-170 Ma, 142.3-137.3 Ma and 130-123.3 Ma. These peaks correlate with increases in the number of linkage events at the fault tips, though not always in the central section. For example, there is no increase in linkage events in the central section coeval with the throw-rate increase between 142.3 and 137.3 Ma (Fig 5d). This contrasts with the fault tips, where an increase in linkage events is observed during this time interval (Fig 5c, e).

### **5 Discussion**

### 5.1 Conceptual model of dip-linkage

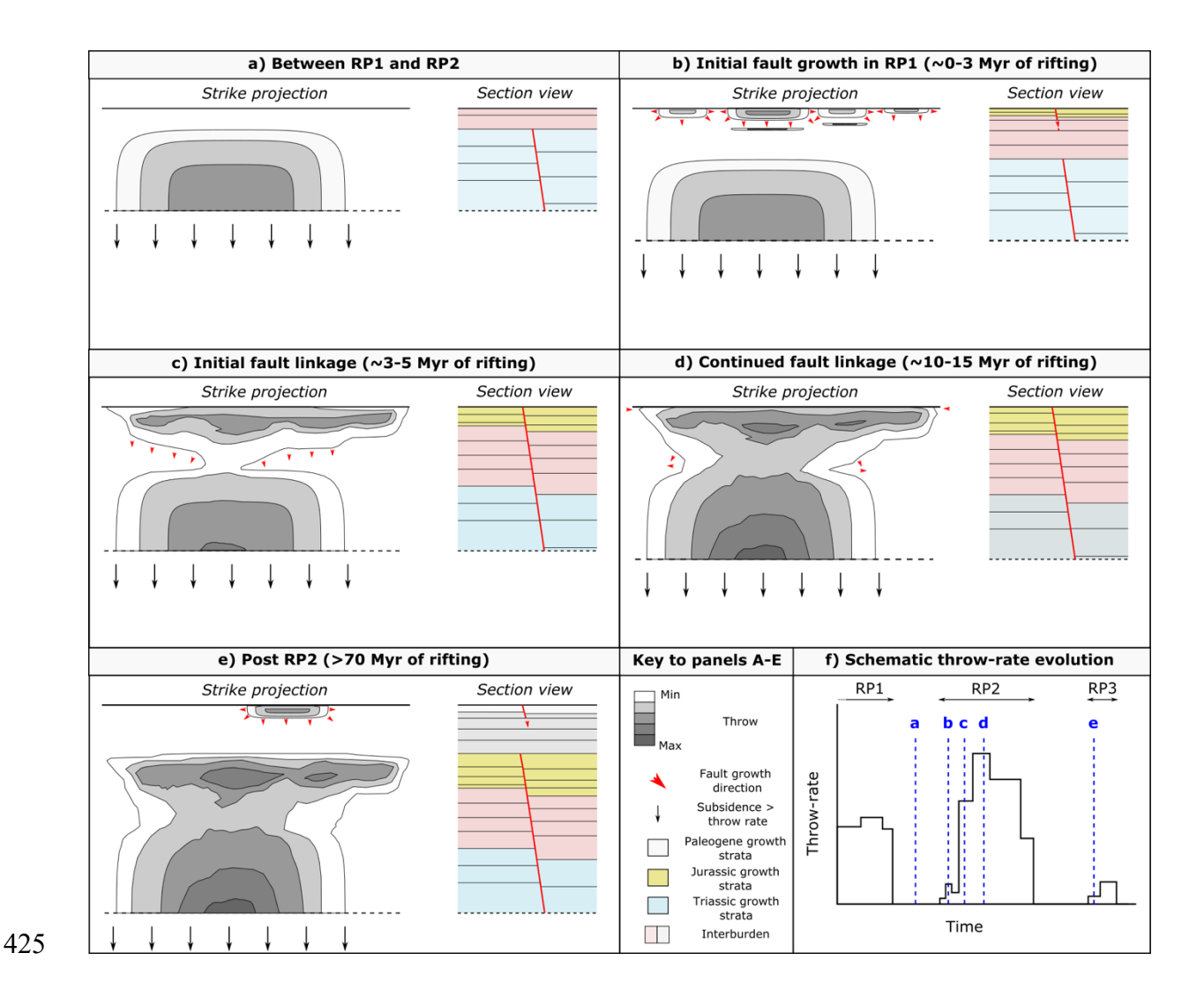


Figure 6: Schematic outlining the progressive dip-linkage observed on our studied faults. A-E) Conceptual model of fault growth and dip-linkage across multiple rift phases. F) Schematic throw-rate evolution showing the time represented by panels A-E. See text for further discussion.

We use 3D seismic reflection and borehole data to examine the evolution of two normal faults on the Exmouth Plateau. We present here a new 5-stage model highlighting the key

role played by dip linkage on growth of the faults, and the relationship this has to throw rate variability (Fig 6). We also explore some of the controls on fault behaviour.

Stage 1: Lower to Middle Triassic rifting & inter-rift phase (Fig. 6a): The deepest mapped stratigraphic packages adjacent to both faults exhibit growth, indicating only the final stages of Early to Middle Triassic rifting is imaged within our dataset (Fig. 4, 5). Consistent with Bilal and McClay (2022), rifting mostly ceased before the Norian (Late Triassic; i.e. the 220 Ma horizon), although the exact timing of rift cessation remain uncertain within our specific dataset due to limited age controls at this level (Fig 1, 2). The 220 Ma horizon is overlain by variably thick, undeformed Mungaroo Formation, with thickness changes attributed to along-strike differences in when F1 and F2 became inactive, and to regional variations in sediment accumulation and subsidence rates (Bilal and McClay, 2022).

Stage 2: Initiation of fault growth during Jurassic rifting (Fig. 6b): During the initial stages of Jurassic rifting, small faults formed (<2 km in length based on slip-rate profiles; Fig. S7, S11). Fault nucleation locally occurred within the Mungaroo Formation between ~100 and 150 m above the pre-existing fault and below the free surface, causing monoclines to develop at the latter (Fig 5b). The alignment of Jurassic faults above Lower to Middle Triassic fault traces suggests pre-existing faults controlled the location of subsequent faults prior to linkage (Collanega et al., 2019; Duffy et al., 2015; Jitmahantakul et al., 2024), with the angle between extension direction and pre-existing faults affecting the morphology of later fault networks (Duffy et al., 2017, 2015; Samsu et al., 2023; Zwaan et al., 2016). Unlike many basement features where the basement fault propagates upwards, resulting in a gradual upward decrease in throw above the lowermost growth packages (Collanega et al., 2019; Phillips et al., 2019), the presence of the throw minima directly above the Lower to Middle Triassic growth strata suggests that Jurassic faults likely propagated downwards

towards Lower to Middle Triassic faults. Should this be the case, the lower, pre-existing fault was unable to propagate upwards, perhaps due to ductile deformation within intervening, mechanically weak material (e.g., mudstone).

456

457

458

459

460

461

462

463

464

465

466

467

468

469

470

471

472

473

474

475

476

477

478

# Stage 3 - Initial linkage of Jurassic and Lower to Middle Triassic faults (Fig. 6c): During continued Jurassic rifting, the down-dip propagation of the Jurassic faults, or the updip propagation of pre-existing faults resulted in dip-linkage. For F1, initial linkage occurred where the intervening stratigraphic thickness was relatively thin (<150 m), Triassic throw was greatest, and the period of active faulting longer (Fig. 4); although because the full length of F1 is not imaged, it is not possible to define the along-strike linkage patterns towards the fault tips. For F2, linkage began near the centre, where throw maxima across both Triassic and Jurassic horizons were located close to the centre of the fault (Fig. 6). Fault linkage was temporally associated with an increase in slip-rate and a change in the shape of the throw-rate profile (Fig 4, 5, 6f). Ideal throw-rate profiles are either elliptical or triangular, with maximum throw rate (and ultimately throw) located in the centre of the fault. It is expected that where the extension direction between rift phases is similar (i.e., ESE to WNW in the study area (Bilal and McClay, 2022), faults are more likely to be reactivated, although our data shows this does not occur at the same time across the whole fault (Fig 4, 5). For example, the shape of the throw-rate profile for F1 during the early stages of linkage (213-209 Ma), was bi-modal, with high values recorded to the south of the profile (Figure S9). As progressive linkage occurs, different patches of the fault link and the related throw-rate increases, causing the shape of the throw profile to gradually evolve towards the approximately triangular profile presently observed across Jurassic horizons (Fig 4, 5, S4, S9).

Stage 4 - Continued fault linkage (Fig 6d): As throw continued to accumulate, the proportion of the fault that had undergone dip-linkage increases (Fig 4, 5). During Stage 4, the linkages ages for F2 displayed an 'elliptical' shape, with linkage occurring rapidly near the centre of the fault, as indicated by the cluster of linkage events between 200 and 220 Myr, and a more protracted linkage history near the faults tip, with linkage events recorded across the duration of Triassic rifting (Fig 5b). Similar to previous studies (Lathrop et al., 2021; Meyer et al., 2002; Nicol et al., 2020), during the later stages of Jurassic rifting, F2 shows evidence of tip retreat, where the fault loses ~10% of its maximum length (Figure S9b,c). Lateral tip retreat has been previously documented where large offset faults lose up to 25% of their surface trace during the final 25% of fault slip (Lathrop et al., 2021). This has been attributed to strain being concentrated towards the centre of the fault (Lathrop et al., 2021), which in this and possibly other cases could be controlled by an increased proportion of diplinkage during this time period in this location. The maximum dip-linkage gradient corresponds with a large increase in slip rate (Fig 4c-d, 5c-e). This could be caused by two factors, either an increase in the rate of tectonic loading on the fault, or linkage itself causing an increase in slip rate. There is no far-field tectonic events that can be directly connected to increases in throw-rate (Bilal and McClay, 2022), so although it is difficult to deduce the full breakup history of the Exmouth Plateau (Lathrop et al., 2021), plate-scale tectonic forces are unlikely to be the cause of the throw rate acceleration. Our favoured explanation is that linkage itself causes the throw rate acceleration across both faults. This is because dip-linkage increases the fault area, enabling earthquakes with larger magnitude to occur (Wells and Coppersmith, 1994). Accruing slip on a hardlinked fault is also likely to be more energetically favourable than on a segmented fault. Depth-linkage enables earthquake ruptures to cross segmented faults (Ulrich et al., 2019), and

479

480

481

482

483

484

485

486

487

488

489

490

491

492

493

494

495

496

497

498

499

500

501

as rifts evolve, segmented faults are known to coalesce, concentrating slip onto a subset of the fault network (Neuharth et al., 2022; Nixon et al., 2024).

503

504

505

506

507

508

509

510

511

512

513

514

515

516

517

518

519

520

521

522

523

524

525

Stage 5 - Post Jurassic rifting (Fig 6d): Following Jurassic rifting, F1 continued to accumulate throw along its full length, while F2 entered a period of quiescence before experiencing renewed growth during the Paleogene. During Paleogene rifting, new faults nucleated in the shallow sub-surface and gradually linked to Jurassic faults, suggesting the stages described above can occur multiple times in areas affected by multiple rifting episodes. 5.2 Implications of dip-linkage on fault growth, earthquake behaviour and seismic hazard Traditional models of fault growth emphasise the relationships between fault length and maximum throw or displacement (e.g., Rotevatn et al., 2019). Our data from F2 supports the widely accepted two-phase growth model of rapid lengthening followed by throw accumulation. However, our results also highlight the critical role of down-dip fault growth and linkage in controlling temporal changes in throw and slip rate. In multi-phase rift settings, slip-rate evolution appears to reflect a complex interplay between throw accumulated on pre-existing faults during previous rifting, the spatial location of the reactivated fault, and the stratigraphic thickness between the pre-existing and new fault. A broader regional assessment using similar methods would help determine the generality of these controls and refine models of fault interaction and growth across the Exmouth Plateau and other similar regions. Our study has demonstrated that dip-linkage is contemporaneous with an increase in slip-rate (Fig 4, 5). A consequence of dip-linkage is that the fault has a much larger potential surface area, therefore also increasing the potential earthquake rupture patch and likelihood of larger

earthquakes (Shearer, 2019). We find linkage progresses along a single fault, with rapid

linkage near the centre of a fault, followed by more protracted linkage towards its tips. This causes not only a change in fault size and potential slips patches, but also in the proportion of the pre-existing fault that has a direct link to the surface. This effects the shape of the slip-rate profiles, which has been shown to additionally influence the seismic hazard posed by a fault (Faure Walker et al., 2019). Due to data availability, probabilistic seismic hazard assessment (PSHA), and physics based models (PBSH), often rely on the surface trace of the fault, and slip-rates often calculated at a single point on the fault (e.g., Pace et al., 2016; Valentini et al., 2017). In our study area, F1 and F2 remained a constant length during fault linkage, with F2 slightly reducing in length during the latter stages of linkage (Fig 4, 5) (e.g., Lathrop et al. 2021). Using empirical relationships, we would predict that the maximum magnitude of an earthquake on F2 would reduce following dip-linkage as fault length decreases (Wells and Coppersmith, 1994). Put another way, a failure to recognise an increase in slip-rate would lead to the erroneous conclusion that the seismic hazard posed by F2 was decreasing, when in fact it was increasing due to the increased slip-rate and likelihood for surface-rupturing earthquakes. As dip-linkage has been found to progress along a single fault (Fig 4, 5), it can reasonably be suggested that linkage will not occur at the same time on each fault across a kinematically linked fault network. We therefore suggest that dip-linkage can influence the magnitude and spatial distribution of slip, and therefore the resultant seismic hazard across an evolving fault network developing above pre-existing faults. Several regions of active continental extension, such as Greece (Cavinato and Celles, 1999; Ford et al., 2017) and Italy, have undergone multiple deformation events, with the active

526

527

528

529

530

531

532

533

534

535

536

537

538

539

540

541

542

543

544

545

546

547

548

549

550

Ford et al., 2017) and Italy, have undergone multiple deformation events, with the active extension over the last <5 Myrs interacting with the pre-existing structural fabric. Our research indicates that dip-linkage can occur over >20 Myrs, raising the possibility that faults in these regions that have not already undergone dip-linkage may still be in the process of linking to pre-existing structures. Indeed, active normal faults are often under displaced when

compared to global displacement/length scaling relationships (Lathrop et al., 2022), a characteristic that would match our suggested fault growth model whereby length is established relatively early, but that dip-linkage has not yet occurred. It should be noted, however, that the throw-rates observed across the NW Shelf are lower (i.e., <0.05 mm/yr) than those observed in many actively extending regions (i.e., 0.03 to 0.2 mm/yr; Nicol et al., 1997) and that dip-linkage may be expected to occur quicker in areas with greater throw-rates. Dip-linkage affects key input parameters for PSHA and may occur in pulses that last a few million years (Fig 4, 5). Therefore, the seismic hazard of individual faults and fault networks may increase over similar timescales.

### 560 Conclusions

Our work has demonstrated that the detailed analysis of faults with multiple down-dip throw maxima can provide insights into the timing of dip-linkage. By studying two normal faults, we find that dip-linkage does not occur at the same time along the length of a single fault but instead spans a period of ~20 Myr, with a more protracted linkage history recorded towards the tips of the faults. We suggest that linkage age is influenced by an interplay between Lower to Middle Triassic throw accumulation, Jurassic throw accumulation rate, position along the Jurassic fault, and the interburden thickness. Dip-linkage increases the connected area of the fault and was found to be associated with an acceleration in throw rate for segments of the fault where linkage occurred. We argue that dip-linkage should be considered in fault growth models of multi-phase rift systems and that a similar method can be used to better understand how fault linkage evolves across a fault network. Because dip-linkage causes an increase in slip-rate, the potential for dip-linkage should be considered when assessing the long-term seismic hazard of actively extending regions.

## **References (66 / 70)**

575	Andrews, B.J., Mildon, Z.K., Jackson, C.A.L., Bond, C.E., 2024. Quantifying fault interpretation
576	uncertainties and their impact on fault seal and seismic hazard analysis. Journal of
577	Structural Geology 184, 105158. https://doi.org/10.1016/j.jsg.2024.105158
578	Barrett, B.J., Hodgson, D.M., Jackson, C.AL., Lloyd, C., Casagrande, J., Collier, R.E.L., 2021.
579	Quantitative analysis of a footwall-scarp degradation complex and syn-rift
580	stratigraphic architecture, Exmouth Plateau, NW Shelf, offshore Australia. Basin
581	Research 33, 1135–1169. https://doi.org/10.1111/bre.12508
582	Bilal, A., McClay, K., 2022. Tectonic and stratigraphic evolution of the central Exmouth
583	Plateau, NW Shelf of Australia. Marine and Petroleum Geology 136, 105447.
584	https://doi.org/10.1016/j.marpetgeo.2021.105447
585	Black, M., McCormack, K.D., Elders, C., Robertson, D., 2017. Extensional fault evolution
586	within the Exmouth Sub-basin, North West Shelf, Australia. Marine and Petroleum
587	Geology 85, 301–315. https://doi.org/10.1016/j.marpetgeo.2017.05.022
588	Cavinato, G.P., Celles, P.G.D., 1999. Extensional basins in the tectonically bimodal central
589	Apennines fold-thrust belt, Italy: Response to corner flow above a subducting slab in
590	retrograde motion. Geology 27, 955–958. https://doi.org/10.1130/0091-
591	7613(1999)027<0955:EBITTB>2.3.CO;2
592	Childs, C., Manzocchi, T., Nicol, A., Walsh, J.J., Soden, A.M., Conneally, J.C., Delogkos, E.,
593	2017. The relationship between normal drag, relay ramp aspect ratio and fault zone

594	structure. Geological Society, London, Special Publications 439, 355–372.
595	https://doi.org/10.1144/SP439.16
596	Collanega, L., Siuda, K., AL. Jackson, C., Bell, R.E., Coleman, A.J., Lenhart, A., Magee, C.,
597	Breda, A., 2019. Normal fault growth influenced by basement fabrics: The
598	importance of preferential nucleation from pre-existing structures. Basin Research
599	31, 659-687. https://doi.org/10.1111/bre.12327
600	Coppersmith, K.J., 1988. Temporal and Spatial Clustering of Earthquake Activity in the
601	Central and Eastern United States. Seismological Research Letters 59, 299–304.
602	https://doi.org/10.1785/gssrl.59.4.299
603 604	Dawers, N.H., Anders, M.H., 1995. Displacement-length scaling and fault linkage. Journal of Structural Geology 17, 607–614. https://doi.org/10.1016/0191-8141(94)00091-D
605	Delogkos, E., Manzocchi, T., Childs, C., Camanni, G., Roche, V., 2020. The 3D structure of a
606	normal fault from multiple outcrop observations. Journal of Structural Geology 136,
607	104009. https://doi.org/10.1016/j.jsg.2020.104009
608	Deng, C., Fossen, H., Gawthorpe, R.L., Rotevatn, A., Jackson, C.AL., FazliKhani, H., 2017.
609	Influence of fault reactivation during multiphase rifting: The Oseberg area, northern
610	North Sea rift. Marine and Petroleum Geology 86, 1252–1272.
611	https://doi.org/10.1016/j.marpetgeo.2017.07.025

612	Deng, H., McClay, K., 2021. Three-dimensional geometry and growth of a basement-involved
613	fault network developed during multiphase extension, Enderby Terrace, North West
614	Shelf of Australia. GSA Bulletin 133, 2051–2078. https://doi.org/10.1130/B35779.1
615	Deng, H., McClay, K., 2019. Development of extensional fault and fold system: Insights from
616	3D seismic interpretation of the Enderby Terrace, NW Shelf of Australia. Marine and
617	Petroleum Geology 104, 11–28. https://doi.org/10.1016/j.marpetgeo.2019.03.003
618	Deng, H., McClay, K., Bilal, A., 2021. Multiphase activation of the boundary fault system of
619	the eastern Dampier subbasin, Northwest Shelf of Australia. AAPG Bulletin 105, 157–
620	188. https://doi.org/10.1306/03022019160
621	Deng, H., McClay, K., Hanlin, C., Finch, E., Jablonski, D., Jitmahantakul, S., 2024. Structural
622	inheritance controls crustal-scale extensional fault-related folding in the Exmouth
623	and Dampier Sub-basins, North West Shelf, Australia. AAPG Bulletin 108, 1291–1326.
624	https://doi.org/10.1306/01242423035
625	Direen, N.G., Stagg, H.M.J., Symonds, P.A., Colwell, J.B., 2008. Architecture of volcanic rifted
626	margins: new insights from the Exmouth – Gascoyne margin, Western Australia.
627	Australian Journal of Earth Sciences 55, 341–363.
628	https://doi.org/10.1080/08120090701769472
629	Dolan, J.F., Bowman, D.D., Sammis, C.G., 2007. Long-range and long-term fault interactions
630	in Southern California. Geology 35, 855–858. https://doi.org/10.1130/G23789A.1

631	Duffy, O.B., Bell, R.E., Jackson, C.AL., Gawthorpe, R.L., Whipp, P.S., 2015. Fault growth and
632	interactions in a multiphase rift fault network: Horda Platform, Norwegian North Sea.
633	Journal of Structural Geology 80, 99–119. https://doi.org/10.1016/j.jsg.2015.08.015
634	Duffy, O.B., Nixon, C.W., Bell, R.E., Jackson, C.AL., Gawthorpe, R.L., Sanderson, D.J., Whipp,
635	P.S., 2017. The topology of evolving rift fault networks: Single-phase vs multi-phase
636	rifts. Journal of Structural Geology 96, 192–202.
637	https://doi.org/10.1016/j.jsg.2017.02.001
638	Etheridge, M.A., O'Brien, G.W., 1994. Structural and Tectonic Evolution of the Western
639	Australian Margin Basin System.
640	Faure Walker, J.P., Visini, F., Roberts, G., Galasso, C., McCaffrey, K., Mildon, Z., 2019. Variable
641	Fault Geometry Suggests Detailed Fault-Slip-Rate Profiles and Geometries Are
642	Needed for Fault-Based Probabilistic Seismic Hazard Assessment (PSHA). Bulletin of
643	the Seismological Society of America 109, 110–123.
644	https://doi.org/10.1785/0120180137
645	Ford, M., Hemelsdaël, R., Mancini, M., Palyvos, N., 2017. Rift migration and lateral
646	propagation: evolution of normal faults and sediment-routing systems of the western
647	Corinth rift (Greece). Geological Society, London, Special Publications 439, 131–168.
648	https://doi.org/10.1144/SP439.15
649	Gartrell, A.P., 2000. Rheological controls on extensional styles and the structural evolution of
650	the Northern Carnarvon Basin, North West Shelf, Australia. Australian Journal of
651	Earth Sciences 47, 231–244. https://doi.org/10.1046/j.1440-0952.2000.00776.x

652 Holden, N., Alaei, B., Skurtveit, E., Braathen, A., 2024. Implications of depth conversion on 653 fault geometries and fault-risk assessment in the Smeaheia CO2 storage site, 654 northern North Sea. Geoenergy 0, geoenergy 2024-006. 655 https://doi.org/10.1144/geoenergy2024-006 656 Jackson, C.A.-L., Bell, R.E., Rotevatn, A., Tvedt, A.B.M., 2017. Techniques to determine the 657 kinematics of synsedimentary normal faults and implications for fault growth models. 658 Geological Society, London, Special Publications 439, 187–217. 659 https://doi.org/10.1144/SP439.22 660 Jackson, C.A.-L., Rotevatn, A., 2013. 3D seismic analysis of the structure and evolution of a 661 salt-influenced normal fault zone: A test of competing fault growth models. Journal 662 of Structural Geology 54, 215–234. https://doi.org/10.1016/j.jsg.2013.06.012 663 Jitmahantakul, S., Kaewsomwang, P., Sumpaothong, J., Simpson, R., 2024. Inherited 664 extensional faults and bed-parallel slip in Mae Moh Basin, Thailand with implication 665 for basement fabrics. Journal of Structural Geology 179, 105047. 666 https://doi.org/10.1016/j.jsg.2023.105047 667 Kagan, Y.Y., Jackson, D.D., 1991. Long-term earthquake clustering. Geophysical Journal 668 International 104, 117-133. https://doi.org/10.1111/j.1365-246X.1991.tb02498.x 669 Karner, G.D., Driscoll, N.W., 1999. Style, timing and distribution of tectonic deformation 670 across the Exmouth Plateau, northwest Australia, determined from stratal 671 architecture and quantitative basin modelling, in: MacNiocall, C., Ryan, P. (Eds.),

672	Continental Tectonics, Proceedings of the Ocean Drilling Program. Geological Society
673	of London, London, UK, pp. 271–311. https://doi.org/10.2973/odp.proc.sr.122.1992
674	Lathrop, B.A., Jackson, C. aL., Bell, R.E., Rotevatn, A., 2022. Displacement/Length Scaling
675	Relationships for Normal Faults; a Review, Critique, and Revised Compilation. Front.
676	Earth Sci. 10. https://doi.org/10.3389/feart.2022.907543
677	Lathrop, B.A., Jackson, C.AL., Bell, R.E., Rotevatn, A., 2021. Normal Fault Kinematics and the
678	Role of Lateral Tip Retreat: An Example From Offshore NW Australia. Tectonics 40,
679	e2020TC006631. https://doi.org/10.1029/2020TC006631
680	Magee, C., Jackson, C.AL., 2020. Can we relate the surface expression of dike-induced
681	normal faults to subsurface dike geometry? Geology 49, 366–371.
682	https://doi.org/10.1130/G48171.1
683	Mansfield, C.S., Cartwright, J.A., 1996. High resolution fault displacement mapping from
684	three-dimensional seismic data: evidence for dip linkage during fault growth. Journal
685	of Structural Geology 18, 249–263. https://doi.org/10.1016/S0191-8141(96)80048-4
686	Marsh, N., Imber, J., Holdsworth, R.E., Brockbank, P., Ringrose, P., 2010. The structural
687	evolution of the Halten Terrace, offshore Mid-Norway: extensional fault growth and
688	strain localisation in a multi-layer brittle–ductile system. Basin Research 22, 195–214.
689	https://doi.org/10.1111/j.1365-2117.2009.00404.x

690	Meyer, V., Nicol, A., Childs, C., Walsh, J.J., Watterson, J., 2002. Progressive localisation of
691	strain during the evolution of a normal fault population. Journal of Structural
692	Geology 24, 1215–1231. https://doi.org/10.1016/S0191-8141(01)00104-3
693	Mildon, Z.K., Roberts, G.P., Faure Walker, J.P., Beck, J., Papanikolaou, I., Michetti, A.M., Toda,
694	S., Iezzi, F., Campbell, L., McCaffrey, K.J.W., Shanks, R., Sgambato, C., Robertson, J.,
695	Meschis, M., Vittori, E., 2022. Surface faulting earthquake clustering controlled by
696	fault and shear-zone interactions. Nat Commun 13, 7126.
697	https://doi.org/10.1038/s41467-022-34821-5
698	Mouslopoulou, V., Hristopulos, D.T., 2011. Patterns of tectonic fault interactions captured
699	through geostatistical analysis of microearthquakes. Journal of Geophysical Research:
700	Solid Earth 116. https://doi.org/10.1029/2010JB007804
701	Neuharth, D., Brune, S., Wrona, T., Glerum, A., Braun, J., Yuan, X., 2022. Evolution of Rift
702	Systems and Their Fault Networks in Response to Surface Processes. Tectonics 41,
703	e2021TC007166. https://doi.org/10.1029/2021TC007166
704	Nicol, A., Walsh, J., Berryman, K., Nodder, S., 2005. Growth of a normal fault by the
705	accumulation of slip over millions of years. Journal of Structural Geology 27, 327-
706	342. https://doi.org/10.1016/j.jsg.2004.09.002
707	Nicol, A., Walsh, J., Childs, C., Manzocchi, T., 2020. Chapter 6 - The growth of faults, in:
708	Tanner, D., Brandes, C. (Eds.), Understanding Faults. Elsevier, pp. 221–255.
709	https://doi.org/10.1016/B978-0-12-815985-9.00006-0

- Nicol, A., Walsh, J.J., Watterson, J., Underhill, J.R., 1997. Displacement rates of normal faults.
- 711 Nature 390, 157–159. https://doi.org/10.1038/36548
- 712 Nixon, C.W., McNeill, L.C., Gawthorpe, R.L., Shillington, D.J., Michas, G., Bell, R.E., Moyle, A.,
- Ford, M., Zakharova, N.V., Bull, J.M., de Gelder, G., 2024. Increasing fault slip rates
- within the Corinth Rift, Greece: A rapidly localising active rift fault network. Earth and
- 715 Planetary Science Letters 636, 118716. https://doi.org/10.1016/j.epsl.2024.118716
- Pace, B., Visini, F., Peruzza, L., 2016. FiSH: MATLAB Tools to Turn Fault Data into Seismic-
- 717 Hazard Models. Seismological Research Letters 87, 374–386.
- 718 https://doi.org/10.1785/0220150189
- 719 Pan, S., Bell, R.E., Jackson, C.A.-L., Naliboff, J., 2022. Evolution of normal fault displacement
- and length as continental lithosphere stretches. Basin Research 34, 121–140.
- 721 https://doi.org/10.1111/bre.12613
- Peacock, D.C.P., 2002. Propagation, interaction and linkage in normal fault systems. Earth-
- 723 Science Reviews 58, 121–142. https://doi.org/10.1016/S0012-8252(01)00085-X
- Peacock, D.C.P., Sanderson, D.J., 1991. Displacements, segment linkage and relay ramps in
- 725 normal fault zones. Journal of Structural Geology 13, 721–733.
- 726 https://doi.org/10.1016/0191-8141(91)90033-F
- 727 Phillips, T.B., Fazlikhani, H., Gawthorpe, R.L., Fossen, H., Jackson, C.A.-L., Bell, R.E., Faleide,
- J.I., Rotevatn, A., 2019. The Influence of Structural Inheritance and Multiphase

729	Extension on Rift Development, the NorthernNorth Sea. Tectonics 38, 4099–4126.
730	https://doi.org/10.1029/2019TC005756
731	Phillips, T.B., Jackson, C.AL., Bell, R.E., Duffy, O.B., 2018. Oblique reactivation of lithosphere
732	scale lineaments controls rift physiography – the upper-crustal expression of the
733	Sorgenfrei-Tornquist Zone, offshore southern Norway. Solid Earth 9, 403-429.
734	https://doi.org/10.5194/se-9-403-2018
735	Reeve, M.T., Magee, C., Jackson, C. aL., Bell, R., Bastow, I.D., 2022. Stratigraphic record of
736	continental breakup, offshore NW Australia. Basin Research 34, 1220–1243.
737	https://doi.org/10.1111/bre.12656
738	Roche, V., Camanni, G., Childs, C., Manzocchi, T., Walsh, J., Conneally, J., Saqab, M.M.,
739	Delogkos, E., 2021. Variability in the three-dimensional geometry of segmented
740	normal fault surfaces. Earth-Science Reviews 216, 103523.
741	https://doi.org/10.1016/j.earscirev.2021.103523
742	Rotevatn, A., Jackson, C.AL., Tvedt, A.B.M., Bell, R.E., Blækkan, I., 2019. How do normal
743	faults grow? Journal of Structural Geology, Back to the future 125, 174–184.
744	https://doi.org/10.1016/j.jsg.2018.08.005
745	Rykkelid, E., Fossen, H., 2002. Layer rotation around vertical fault overlap zones:
746	observations from seismic data, field examples, and physical experiments. Marine
747	and Petroleum Geology 19, 181–192. https://doi.org/10.1016/S0264-
748	8172(02)00007-7

749	Samsu, A., Micklethwaite, S., Williams, J.N., Fagereng, Å., Cruden, A.R., 2023. Structural
750	inheritance in amagmatic rift basins: Manifestations and mechanisms for how pre-
751	existing structures influence rift-related faults. Earth-Science Reviews 246, 104568.
752	https://doi.org/10.1016/j.earscirev.2023.104568
753	Shearer, P.M., 2019. Introduction to Seismology. Cambridge University Press.
754	Sun, S., Zou, H., Niu, C., Ren, H., 2022. Lateral and vertical growth and linkage of normal
755	faults in Bozhong8-4 structure of Western Bozhong Sag, Bohai Bay Basin, China.
756	Journal of Structural Geology 164, 104731.
757	https://doi.org/10.1016/j.jsg.2022.104731
758	Ulrich, T., Gabriel, AA., Ampuero, JP., Xu, W., 2019. Dynamic viability of the 2016 Mw 7.8
759	Kaikōura earthquake cascade on weak crustal faults. Nat Commun 10, 1213.
760	https://doi.org/10.1038/s41467-019-09125-w
761	Valentini, A., Visini, F., Pace, B., 2017. Integrating faults and past earthquakes into a
762	probabilistic seismic hazard model for peninsular Italy. Natural Hazards and Earth
763	System Sciences 17, 2017–2039. https://doi.org/10.5194/nhess-17-2017-2017
764	Veevers, J.J., 1988. Morphotectonics of Australia's Northwestern Margin - A Review 19.
765	Walsh, J.J., Watterson, J., 1990. New methods of fault projection for coalmine planning. PYGS
766	48, 209–219. https://doi.org/10.1144/pygs.48.2.209
767	Walsh, J.J., Watterson, J., 1989. Displacement gradients on fault surfaces. Journal of
768	Structural Geology 11, 307–316. https://doi.org/10.1016/0191-8141(89)90070-9

/69	wells, D.L., Coppersmith, K.J., 1994. New empirical relationships among magnitude, rupture
770	length, rupture width, rupture area, and surface displacement. Bulletin of the
771	Seismological Society of America 84, 974–1002.
772	https://doi.org/10.1785/BSSA0840040974
773	Yang, XM., Elders, C., 2016. The Mesozoic structural evolution of the Gorgon Platform,
774	North Carnarvon Basin, Australia. Australian Journal of Earth Sciences 63, 755–770.
775	https://doi.org/10.1080/08120099.2016.1243579
776	Zwaan, F., Schreurs, G., Naliboff, J., Buiter, S.J.H., 2016. Insights into the effects of oblique
777	extension on continental rift interaction from 3D analogue and numerical models.
778	Tectonophysics, Special issue on Tectonics of oblique plate boundary systems 693,
779	239–260. https://doi.org/10.1016/j.tecto.2016.02.036

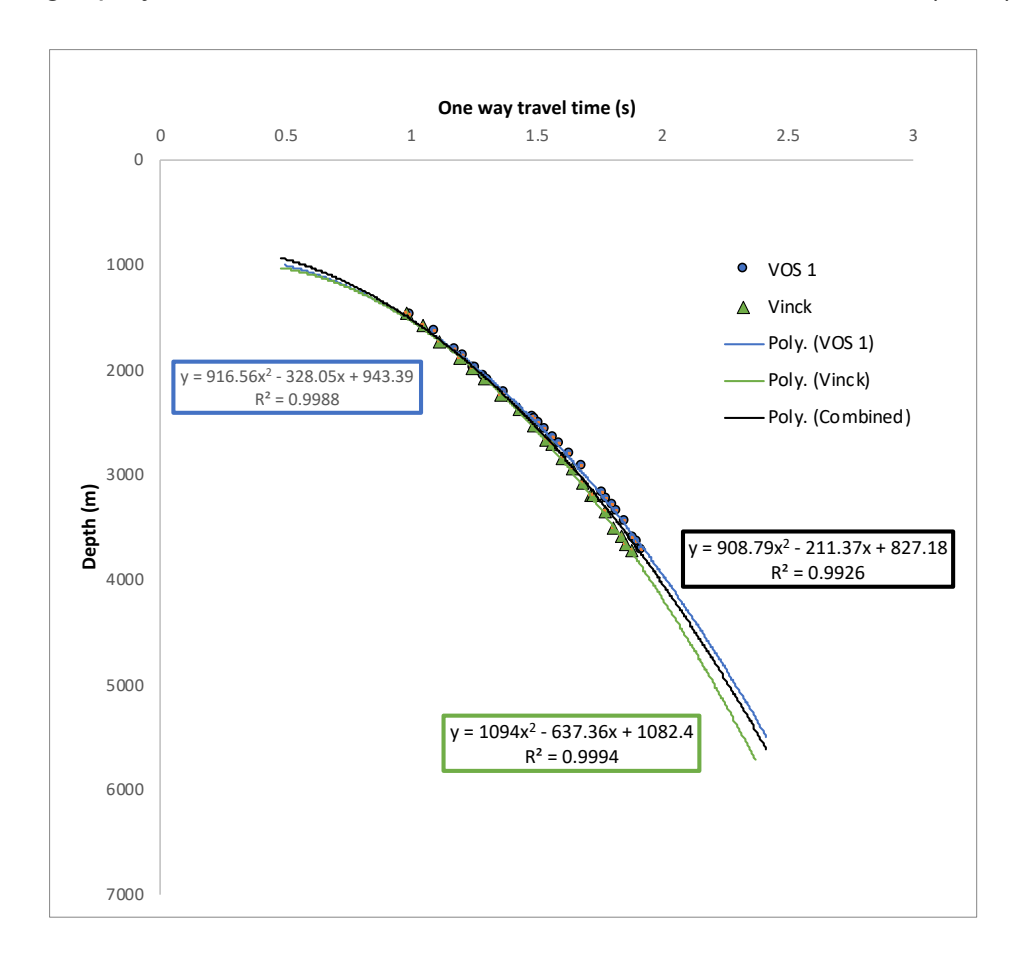
Supplementary information for "Throw rate acceleration caused by dip-linkage on normal faults"

### S1: Depth conversion and its effect on uncertainties in linkage age

The conversion of measured depth values, which are in two-way-time (TWT) to depth in metres, is a considerable source of error in the quantitative throw analysis of faults imaged in seismic data (Holden et al., 2024). This arises because seismic velocities are obtained from borehole data, which effectively provide a 1D snapshot of the subsurface and do not capture spatial variabilities. Additionally, similar to elsewhere in the Exmouth Plateau, wells were drilled in the footwall of normal faults, limiting the depth range and not capturing any potential differences between footwall and hanging wall seismic velocities. Considering the differences between wells for both cubes (below), and the limitations of using check-shot data, we acknowledge a ±10% variation in seismic velocity may occur across the study area.

### S1.1 Agripinna

 The two wells for Agripinna, which contains Fault 1, range in depth from 3717 m and 3730 m, with limited variations in velocities between each well (Table S1). Similarly to Agripinna, we find that a polynomial line of best fit provides the most consistent depth conversion between wells and therefore convert from time to depth by calculating a polynomial line of best fit to the combined check shot data (S1.1).



#### S1.2 Chandon 3D

 The four wells for Chandon3D, which contains Fault 2, range in depth from 1200 m and 3166 m, with limited variations in velocities between each well (Table S1). Similarly to Agripinna, we find that a polynomial line of best fit provides the most consistent depth conversion between wells and therefore convert from time to depth by calculating a polynomial line of best fit to the combined check shot data (S1.2).

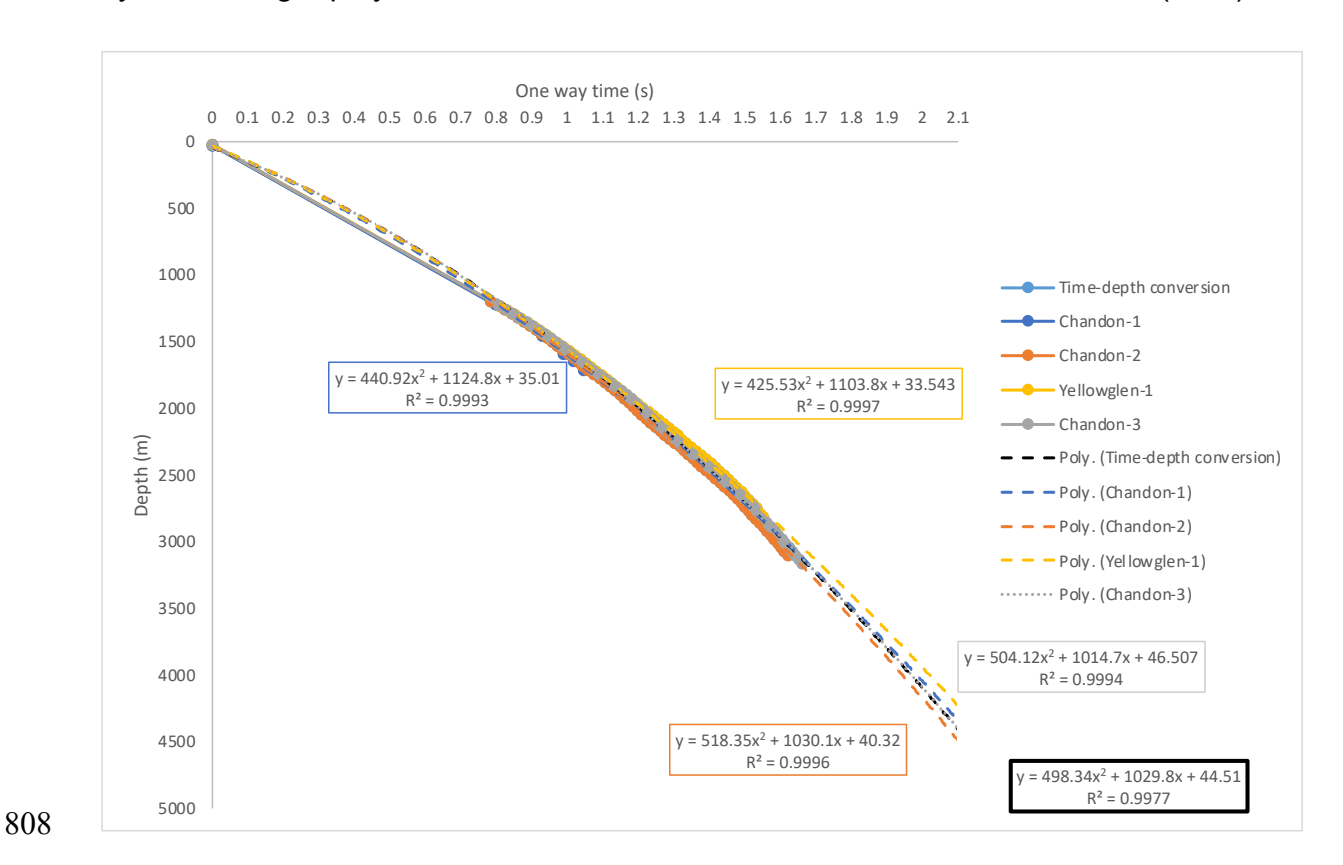


Figure S2: Extrapolated time-depth relationships for the boreholes used to depthconvert measurements made in time (s)

Chandon-1 (Chandon3D)		Chandon-2 (Chandon3D)		Chandon-3 (Chandon3D)		Yellowglen (Chandon3D)		VOS 1 (Agrippina)		Vinck 1 (Agrippina)	
One way time (s)	Measured depth (m)	One way time (s)	Measured depth (m)	One way time (s)	Measured depth (m)	One way time (s)	Measured depth (m)	One way time (s)	Measured depth (m)	One way time (s)	Measured depth (m)
0	28.9	0.000	0022.0	0.000	0022.3	0.000	0022.0	0.992	1483.7	0.979	1469.6
0.797	1225	0.786	1200.3	0.806	1229.6	0.813	1238.0	1.090	1649.7	1.038	1589.6
0.929	1459.7	0.806	1230.5	0.826	1259.9	0.834	1269.1	1.174	1815.7	1.11	1739.6
0.990	1596	0.825	1260.8	0.846	1290.1	0.852	1299.4	1.202	1879.7	1.186	1891.6
1.018	1648.5	0.843	1291.0	0.865	1320.3	0.871	1328.7	1.248	1984.7	1.236	1989.6
1.046	1720	0.861	1321.4	0.883	1350.6	0.889	1358.9	1.254	2000.2	1.286	2095.6

1.173	1929.8	0.879	1351.6	0.901	1380.8	0.906	1389.1	1.284	2068.7	1.355	2241.6
1.220	2053.0	0.896	1381.8	0.919	1411.0	0.923	1419.4	1.302	2107.2	1.421	2389.6
1.255	2143.0	0.912	1412.1	0.936	1441.4	0.940	1449.6	1.366	2231.4	1.485	2541.6
1.362	2348.0	0.928	1442.6	0.952	1471.6	0.956	1479.9	1.479	2462.7	1.534	2664.6
1.371	2405.0	0.943	1472.9	0.968	1501.8	0.972	1510.1	1.486	2481.7	1.553	2716.6
1.403	2475.0	0.958	1503.1	0.983	1532.0	0.989	1540.3	1.505	2518.7	1.6	2842.6
1.434	2548.0	0.973	1533.4	0.998	1562.3	1.006	1570.6	1.533	2585.8	1.636	2947.6
1.476	2642.0	0.988	1563.4	1.013	1592.5	1.022	1600.8	1.561	2647.3	1.681	3092.6
1.489	2680.2	1.003	1593.6	1.028	1622.8	1.037	1631.1	1.589	2714.4	1.712	3190.6
1.507	2714.8	1.017	1623.9	1.043	1653.0	1.053	1661.4	1.631	2817.5	1.716	3199.6
1.513	2748.9	1.031	1654.1	1.058	1683.1	1.068	1691.5	1.675	2932.3	1.719	3208.6
1.587	2943.8	1.045	1684.3	1.073	1713.4	1.082	1721.8	1.760	3182.0	1.766	3364.6
1.606	3022.8	1.059	1714.6	1.088	1743.5	1.097	1752.0	1.773	3235.8	1.803	3502.6
		1.075	1744.8	1.104	1773.7	1.112	1782.3	1.798	3299.4	1.83	3594.6
		1.091	1775.0	1.120	1804.0	1.127	1812.5	1.815	3347.1	1.851	3666.6
		1.106	1805.1	1.135	1834.3	1.142	1842.8	1.847	3458.6	1.87	3729.6
		1.120	1835.4	1.151	1864.7	1.155	1873.0	1.884	3600.8		
		1.134	1865.6	1.166	1894.9	1.169	1903.3	1.899	3646.3		
		1.148	1895.8	1.180	1925.1	1.182	1933.6	1.914	3716.7		
		1.161	1926.0	1.192	1955.4	1.198	1963.8				
		1.174	1956.2	1.204	1985.7	1.213	1993.9				
		1.187	1986.4	1.215	2015.9	1.228	2024.1				
		1.199	2016.7	1.227	2046.1	1.243	2054.5				
		1.210	2047.2	1.238	2076.3	1.257	2084.7				
		1.222	2077.5	1.249	2106.6	1.272	2114.9				
		1.234	2107.7	1.261	2136.8	1.286	2145.2				
		1.248	2138.0	1.275	2167.1	1.299	2175.4				
		1.262	2168.1	1.288	2197.3	1.311	2205.6				
		1.275	2198.4	1.301	2227.6	1.323	2236.0				
		1.289	2228.6	1.314	2257.8	1.335	2266.2				
		1.302	2258.9	1.327	2288.1	1.349	2296.3				
		1.316	2289.0	1.341	2318.3	1.364	2326.5				
		1.329	2319.3	1.355	2348.5	1.378	2356.8				
		1.341	2349.5	1.369	2378.7	1.392	2387.0				
		1.353	2379.7	1.383	2409.0	1.405	2417.3				
		1.365	2410.0	1.396	2439.3	1.417	2447.6				

1.378	2440.3	1.410	2469.5	1.429	2477.8		
1.392	2470.5	1.423	2499.7	1.442	2508.0		
1.405	2500.7	1.436	2530.0	1.454	2538.3		
1.418	2531.1	1.449	2560.2	1.466	2568.5		
1.431	2561.3	1.462	2590.4	1.478	2598.7		
1.444	2591.5	1.475	2620.7	1.490	2628.9		
1.456	2621.8	1.488	2651.0	1.501	2659.2		
1.469	2651.9	1.500	2681.2	1.512	2689.5		
1.481	2682.1	1.513	2711.4	1.523	2719.7		
1.491	2712.4	1.524	2741.6	1.534	2749.9		
1.501	2742.6	1.534	2771.9				
1.511	2772.9	1.544	2802.2				
1.520	2803.2	1.555	2832.4				
1.531	2833.4	1.563	2862.6				
1.542	2863.7	1.574	2892.8				
1.553	2893.9	1.585	2923.1				
1.563	2924.1	1.595	2953.3				
1.573	2954.3	1.605	2983.5				
1.583	2984.6	1.614	3013.8				
1.593	3014.8	1.624	3044.0				
1.602	3045.1	1.634	3074.3				
1.612	3075.3	1.643	3104.5				
1.622	3105.5	1.653	3134.8				
		1.662	3165.0				

Table S1: Checkshot data for all well used in this study.

## **S1.3** Effect of different throw-depth conversions on the extraction of linkage 813 age.

To test the effect of using different depth conversions has on the extraction of linkage age, a throw depth-plot was constructed across Fault 1 using individual well data, combined data, and for all dataset, a polynomial and exponential best fit (Table S2). Based on the resultant throw depth plots (Figure S1.3), the calculated linkage age varied between 200.4 Ma for the combined polynomial relationship, to 204.0 for the combined exponential relationship. In all cases, an exponential relationship provided an older linkage age due to a reduction in throw across the throw minima. Despite this, due to the high throw gradient at the start of rifting, we expect that a different depth conversion would change the absolute linkage ages, but not the overall patterns as discussed in the manuscript. As such, any absolute linkage age

Well	Туре	Relationship	Linkage age (Myr)
Combined	Polynomial	908.79x <sup>2</sup> – 211.37x + 827.18	200.4
Combined	Exponential	577.45e <sup>0.9854x</sup>	204.0
VOS 1	Polynomial	916.56x <sup>2</sup> –328.05x + 943.39	200.7
VOS1	Exponential	594.07e <sup>0.9572x</sup>	202.3
VINCK 1	Polynomial	1094x <sup>2</sup> -637.36x + 1082.4	201.3
VINCK1	Exponential	558.2e <sup>1.0187x</sup>	201.4

# Table S2: Different depth conversions and there effect on the calculation of linkage age.

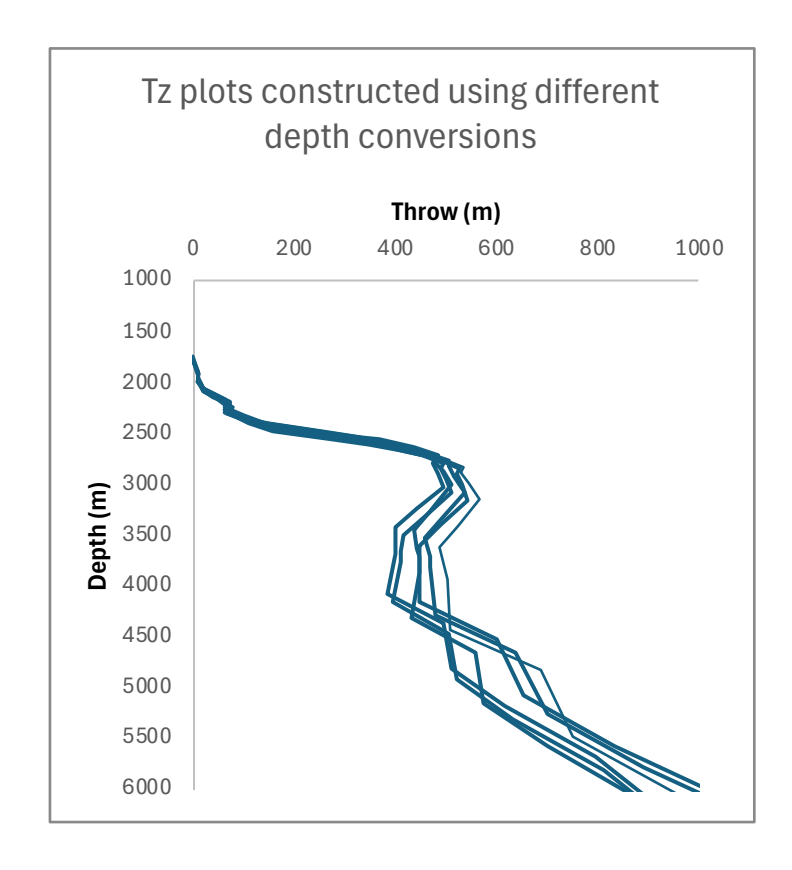
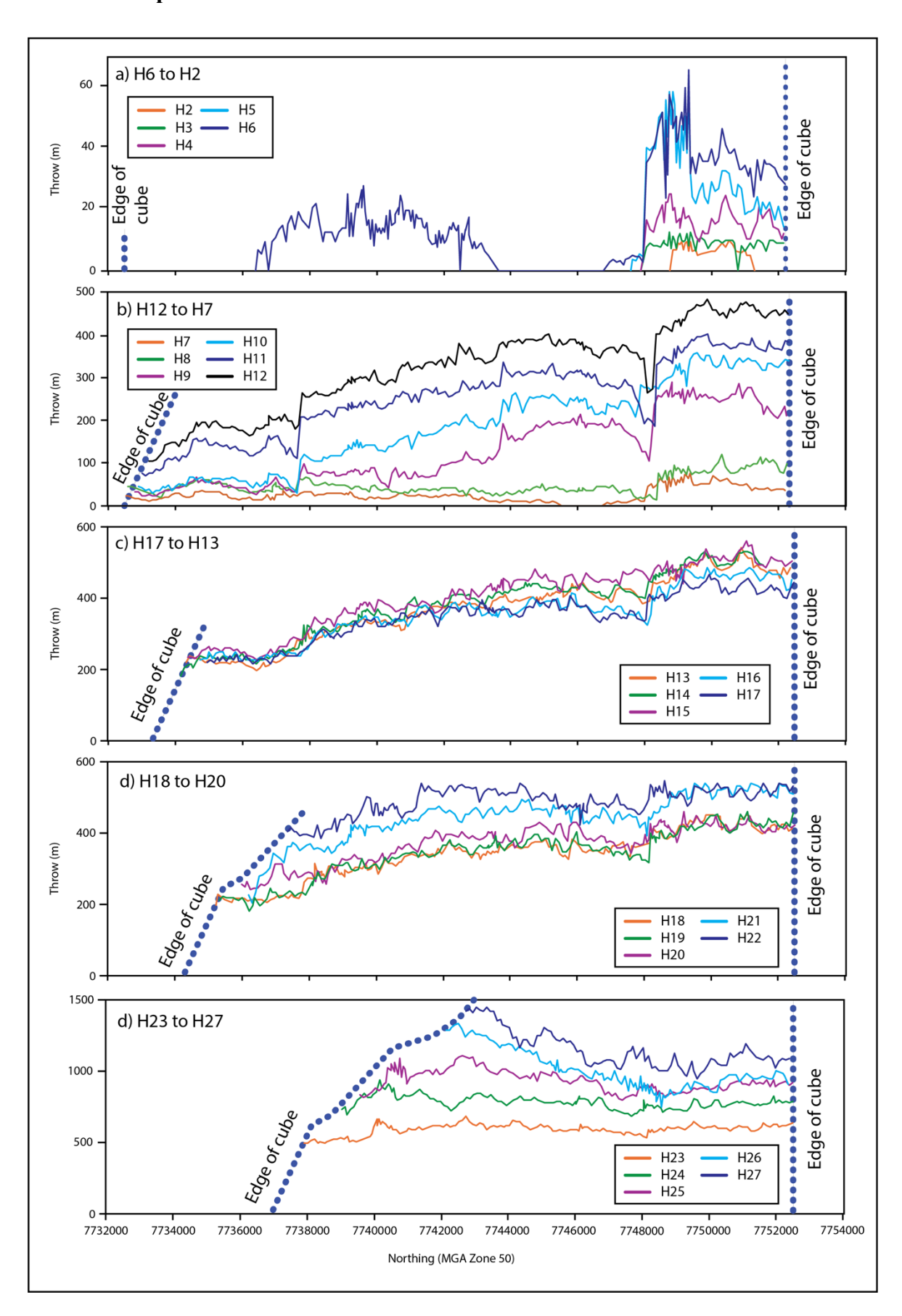


Figure S3: Throw-depth plot constructed based on different depth conversions. Note how very little effect is seen for the shallower depths, but this increases and has a greater effect for the location of fault linkage.

### S2: Throw and throw-rate plots



### S2.2: Throw-rate profiles for Fault 1

836

837

839

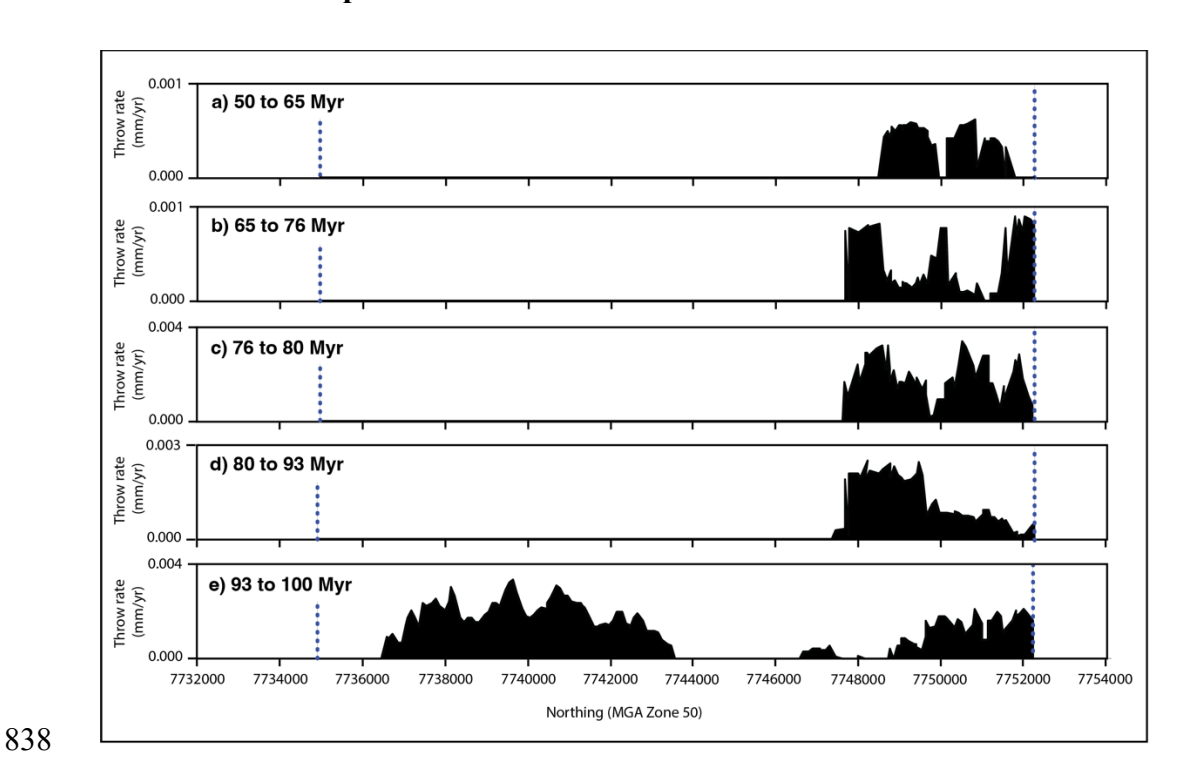


Figure S5: Throw rate profiles for the time periods between 100 and 50 Myr.

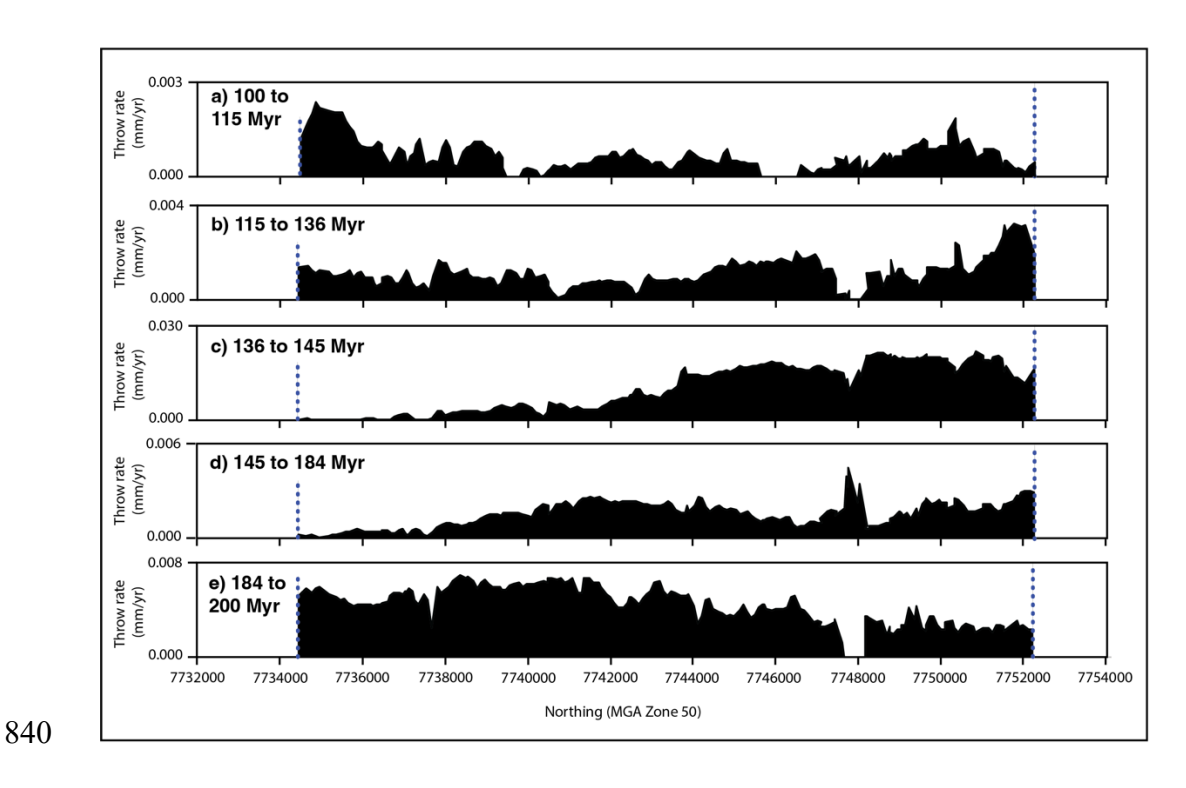


Figure S6: Throw rate profiles for the time periods between 200 and 100 Myr.

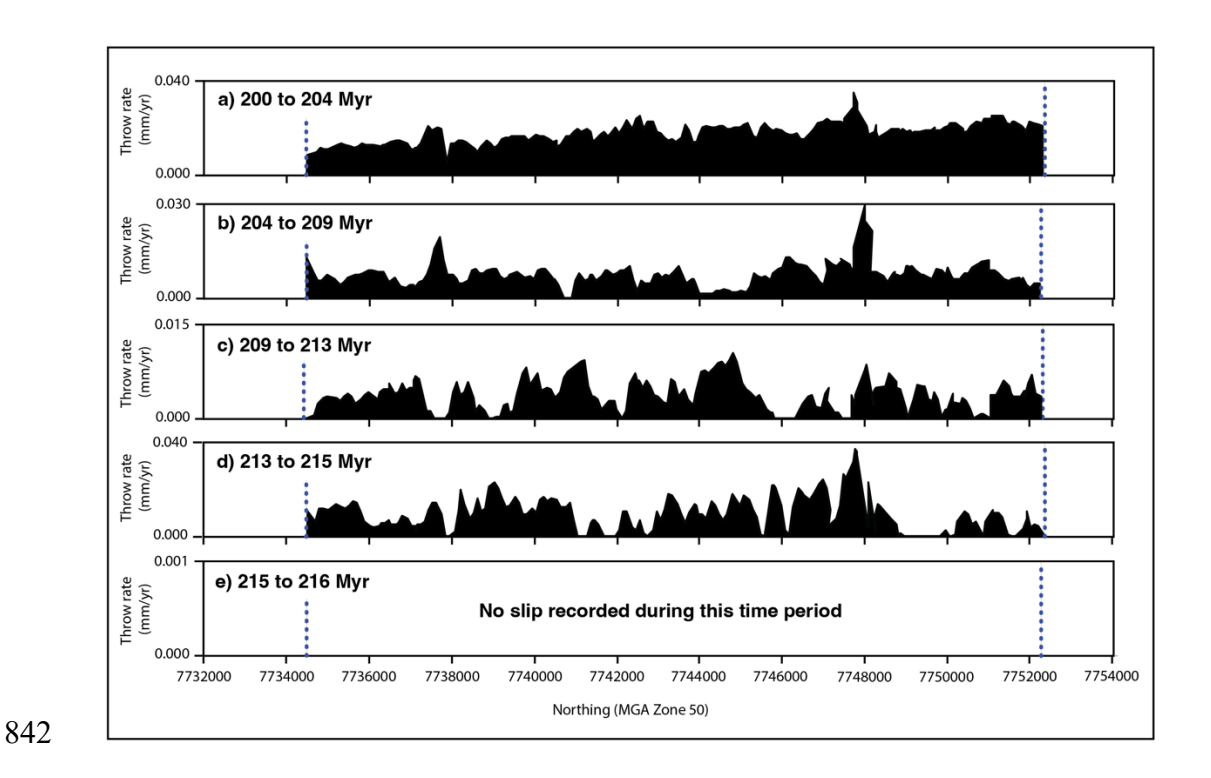


Figure S7: Throw rate profiles for the time periods between 216 and 200 Myr.

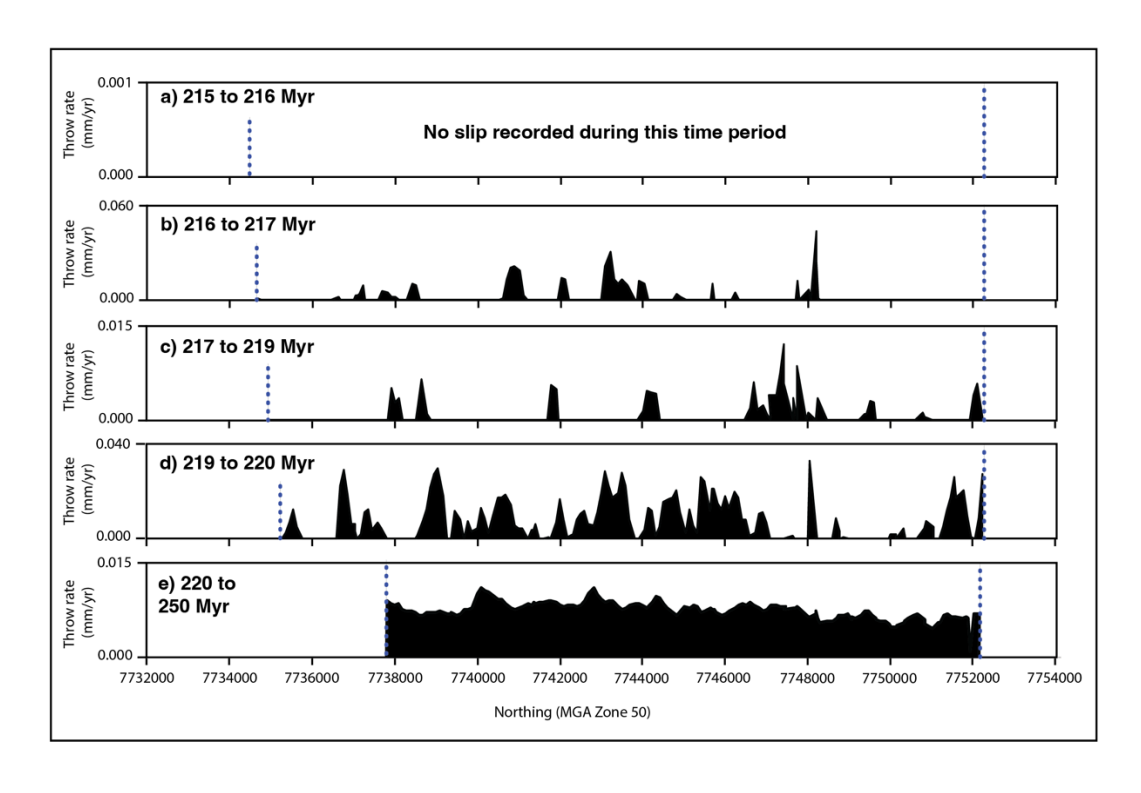


Figure S8: Throw rate profiles for the time periods between 250 and 216 Myr.

### S2.3 Throw profiles for Fault 2

843

844

845

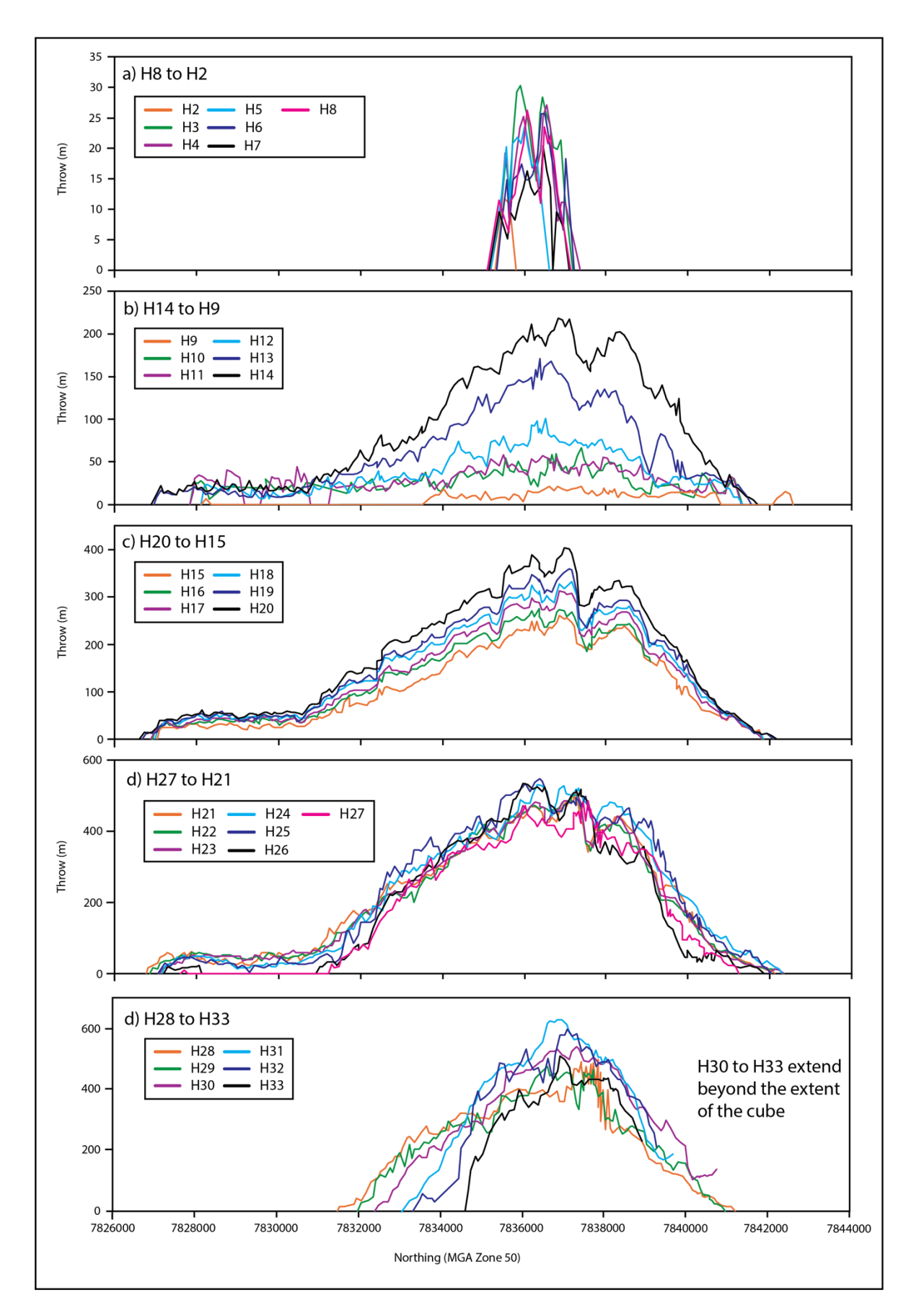


Figure S9: Throw extracted across each horizon for Fault 1.

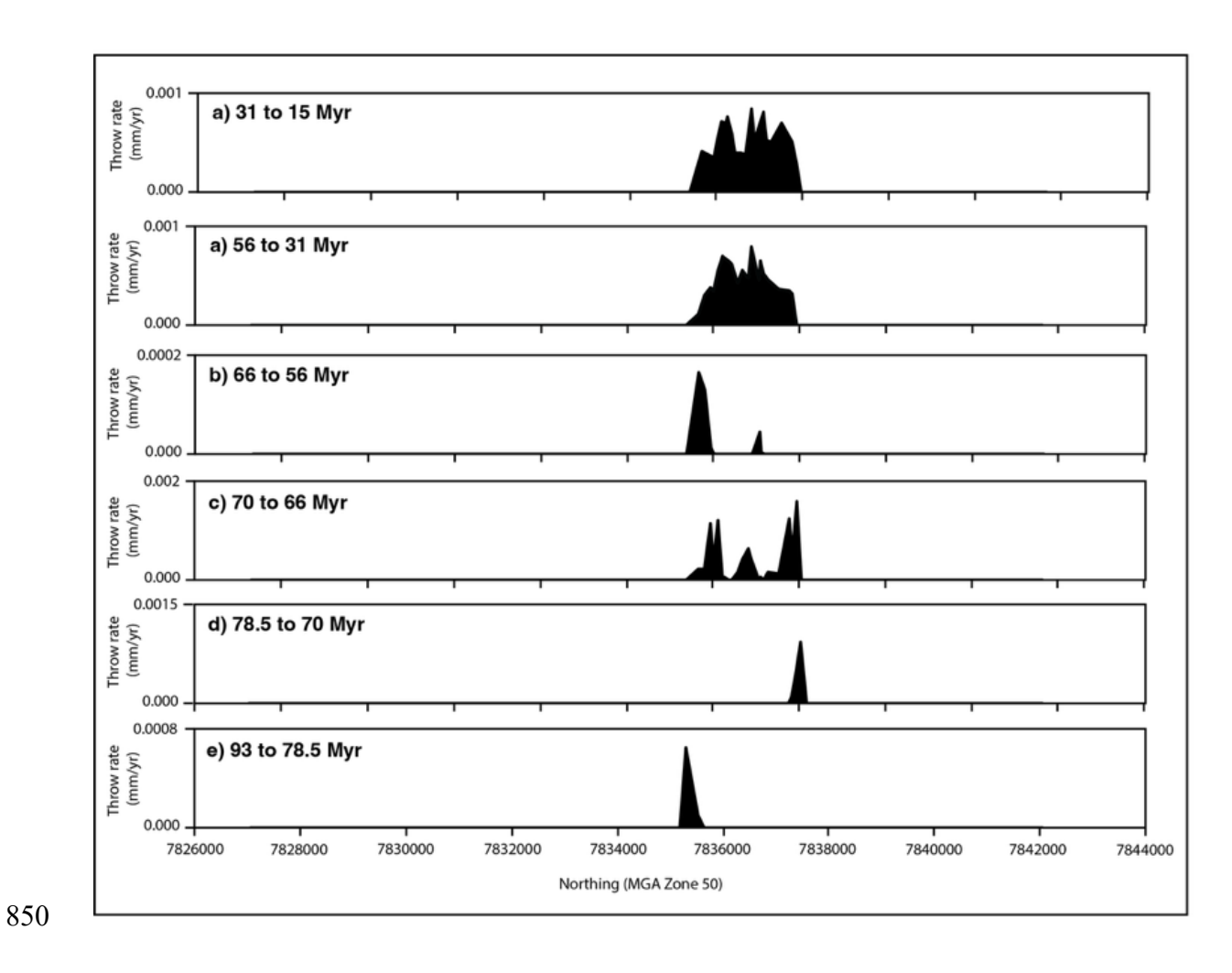


Figure S10: Throw rate profiles for the time periods between 93 and 31 Myr.

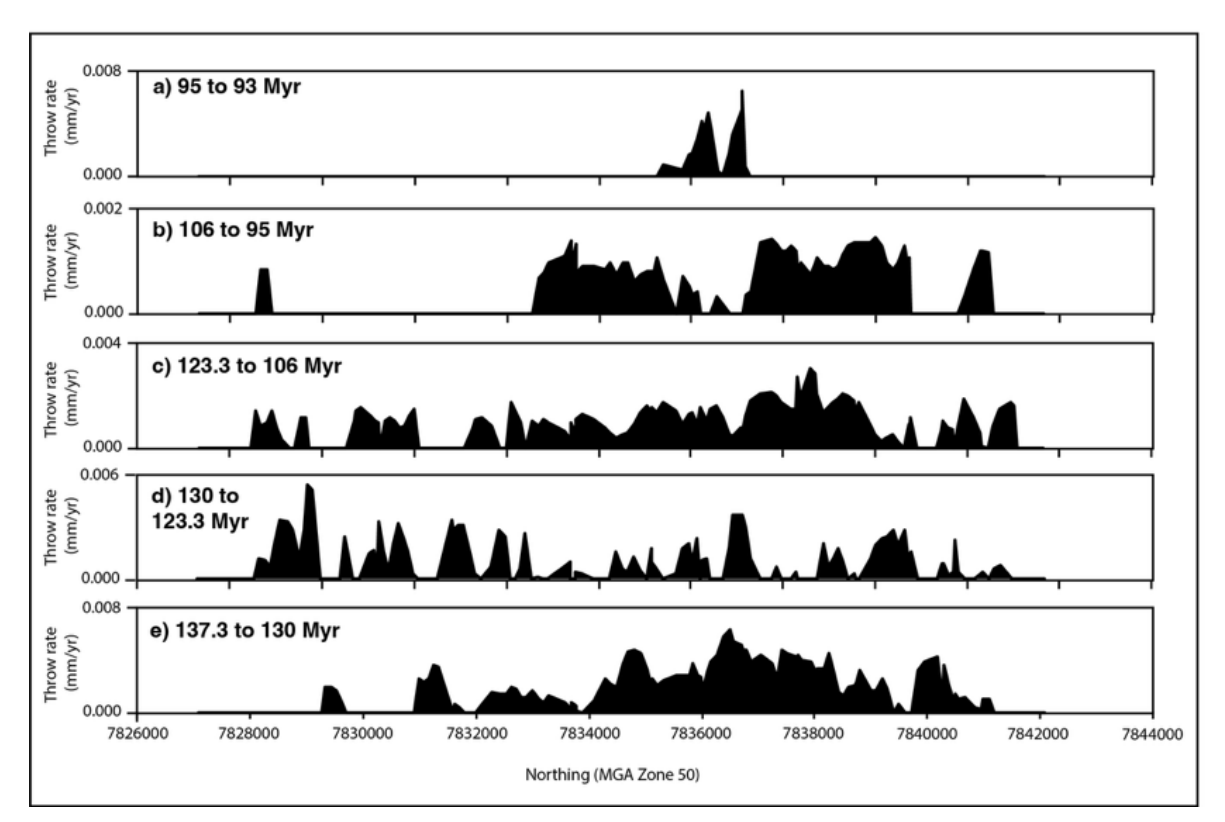


Figure S11: Throw rate profiles for the time periods between 137.3 to 93 Myr.

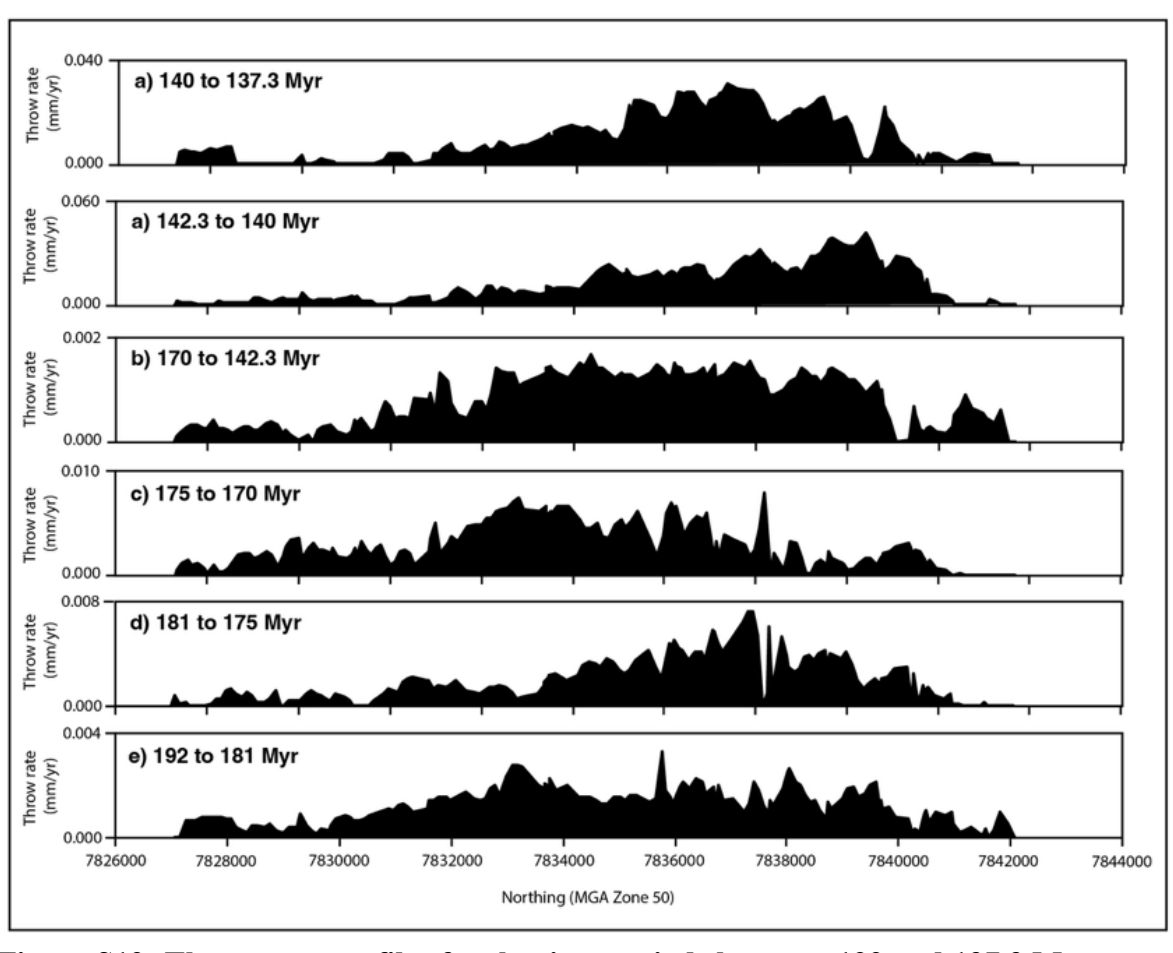


Figure S12: Throw rate profiles for the time periods between 192 and 137.3 Myr.

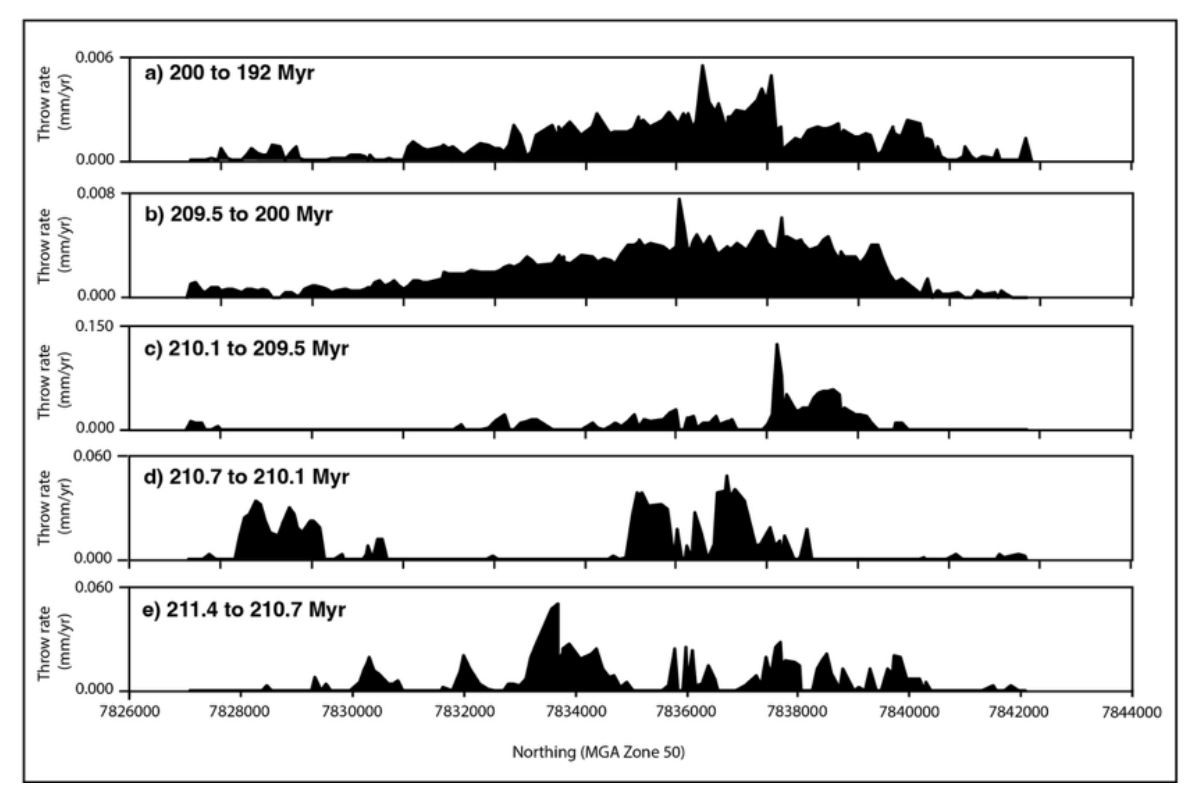


Figure S13: Throw rate profiles for the time periods between 211.4 and 200 Myr.

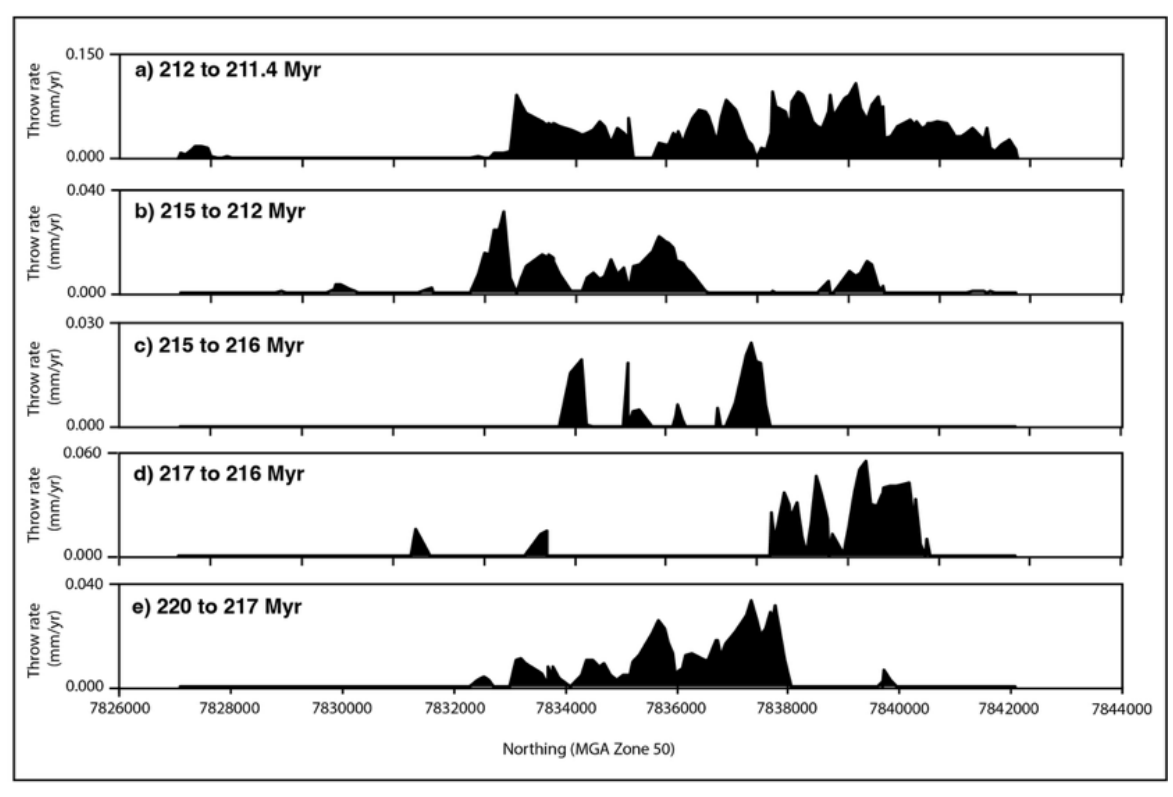


Figure S14: Throw rate profiles for the time periods between 220 and 211.4 Myr.